

1 **Tropical Anvil Clouds: Radiative Driving Towards a**  
2 **Preferred State**

3 **Adam B. Sokol<sup>1</sup>, Dennis L. Hartmann<sup>1</sup>**

4 <sup>1</sup>Department of Atmospheric Sciences, University of Washington, Seattle, WA, USA

5 **Key Points:**

- 6 • Anvil clouds are driven towards a favored structure at which they undergo strong  
7 radiative heating and have a positive radiative effect  
8 • Clouds prone to radiative destabilization have higher concentrations of ice crys-  
9 tals  
10 • The properties of aged cirrus may depend on the time of day at which they were  
11 detrained

---

Corresponding author: Adam B. Sokol, [abs66@uw.edu](mailto:abs66@uw.edu)

**Abstract**

The evolution of anvil clouds detrained from deep convective systems has important implications for the tropical energy balance and is thought to be shaped by radiative heating. We use combined radar-lidar observations and a radiative transfer model to investigate the influence of radiative heating on anvil cloud altitude, thickness, and microphysical structure. We find that high clouds with an optical depth between 1 and 2 are prevalent in tropical convective regions and can persist far from any convective source. These clouds are generally located at higher altitudes than optically thicker clouds, experience strong radiative heating, and contain high concentrations of ice crystals indicative of turbulence. These findings support the hypothesis that anvil clouds are driven towards and maintained at a preferred optical thickness that corresponds to a positive cloud radiative effect. Comparison of daytime and nighttime observations suggests that anvil thinning proceeds more rapidly at night, when net radiative cooling promotes the sinking of cloud top. It is hypothesized that the properties of aged anvil clouds and their susceptibility to radiative destabilization are shaped by the time of day at which the cloud was detrained. These results underscore the importance of small-scale processes in determining the radiative effect of tropical convection.

**Plain Language Summary**

Clouds play an important role in Earth’s energy balance, especially in the tropics. Thick clouds cool the climate by reflecting sunlight, while thinner clouds located high in the atmosphere warm the climate due to their strong greenhouse effect. Tropical thunderstorms generate expansive cloud systems (“anvil” clouds) that initially exert a cooling effect but evolve over time to produce a warming effect. Their net impact on the climate system depends on how much time they spend in their cooling and warming stages. In this study, we use satellite measurements and a radiation model to examine how anvil clouds evolve. We find that anvil clouds with a climate-warming effect are pervasive in the tropics and can be found far from any thunderstorm that would have produced them, suggesting that they are maintained in their warming stage for long periods of time. We observe some unique characteristics of these clouds that provide clues about the processes that maintain them. Our findings provide real-world support for previous hypotheses that, until now, relied on computer simulations. They also highlight the importance of small-scale processes in shaping the large-scale tropical energy balance and underscore the need to consider these processes in projections of future climate change.

**1 Introduction**

Convective clouds play an important role in the energy budget of the tropical atmosphere. Mesoscale convective systems (MCSs) consisting of deep, rainy convective cores and detrained anvil clouds reflect incoming shortwave (SW) radiation and trap outgoing longwave (LW) radiation emitted by Earth’s surface and lower atmosphere. These SW and LW effects are individually strong but nearly cancel each other out on climatological scales. As a result, the net cloud radiative effect (NCRE) in tropical convective regions is near zero (Harrison et al., 1990; Ramanathan et al., 1989; Hartmann et al., 2001). Despite longstanding knowledge of this cancellation, questions remain about its very nature and susceptibility to change. There are compelling reasons to deepen our understanding of convection’s radiative balance: changes to the balance would themselves constitute an important climate feedback (Hartmann, 2016) and could alter patterns in sea surface temperature (Wall et al., 2019), convective aggregation (Bretherton et al., 2005; Wing & Emanuel, 2014), and atmospheric circulation and precipitation (e.g., Randall et al., 1989; Voigt & Shaw, 2015),

The radiative neutrality of tropical convection owes itself to the widespread presence of moderately thick anvil clouds. These clouds exhibit a weakly positive NCRE but

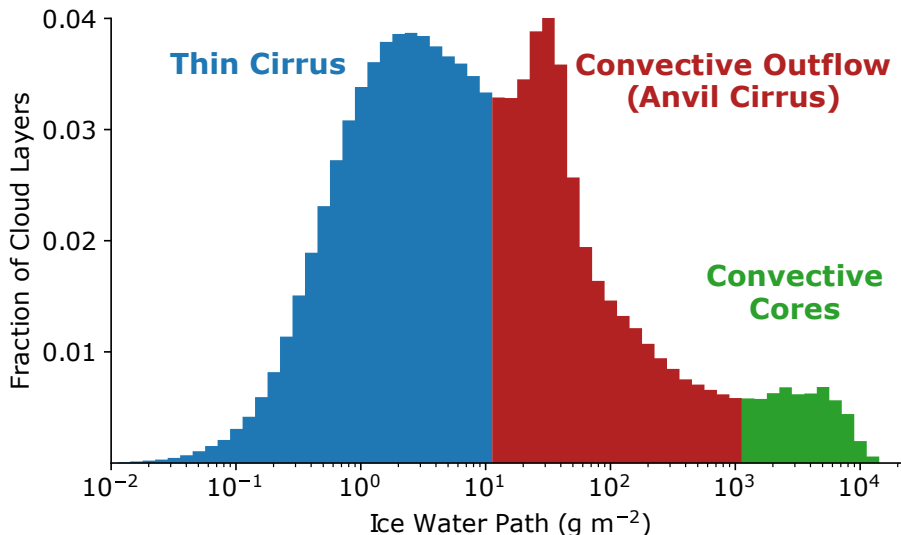


**Figure 1.** Histogram of the ice water path (IWP) of individual cloud layers with tops above 10 km in the tropical western Pacific ( $12^\circ\text{S}$ - $12^\circ\text{N}$ ,  $150^\circ\text{E}$ - $180^\circ\text{E}$ ). Three cloud types are identified for heuristic purposes using the histogram’s two relative minima as boundaries. Layer IWP is calculated using the cloud retrievals described in section 2.1.1 prior correcting for the diurnal cycle of lidar sensitivity (see section 2.1.2). Bin widths are 0.1 in log space.

62 are long lasting and horizontally expansive, allowing them to balance the strongly neg-  
 63 ative NCRE exhibited by deep convective cores and optically thick anvil clouds over a  
 64 smaller area (Hartmann & Berry, 2017). The pervasiveness of moderately thick anvils  
 65 is evident in the observed distribution of ice water path (IWP) of high cloud layers over  
 66 the western Pacific warm pool (Figure 1). The distribution suggests three cloud layer  
 67 categories: deep convective cores, convective outflow (anvil cirrus), and the thin cirrus  
 68 that are characteristic of the tropical upper troposphere. The monotonic increase in fre-  
 69 quency as IWP decreases from  $10^3$  to  $\sim 30$   $\text{g m}^{-2}$  represents the flattening and horizon-  
 70 tal spreading of anvil clouds after they are detrained (Lilly, 1988). If this thinning and  
 71 spreading were to continue indefinitely, one would expect to observe a continued increase  
 72 in frequency as IWP declines from  $30$   $\text{g m}^{-2}$  to the limit of cloud detection. Rather, the  
 73 distribution peaks at  $\sim 30$   $\text{g m}^{-2}$  before falling and rising again to the thin cirrus mode  
 74 at  $\sim 2$   $\text{g m}^{-2}$ . This existence of a peak at  $30$   $\text{g m}^{-2}$  suggests that anvil clouds are pref-  
 75 erentially maintained at that point. Similar bimodality has previously been observed in  
 76 the Southeast Asian monsoon region (Berry & Mace, 2014), but its causes remain largely  
 77 unexplored. To understand how the anvil cloud distribution may change in the future,  
 78 it is necessary to understand the processes that govern the evolution of convective out-  
 79 flow.

80 Radiative heating has long been recognized as an important driver of anvil cloud  
 81 dynamics (Lilly, 1988; Ackerman et al., 1988). Optically thick anvil clouds undergo strong  
 82 LW heating near cloud base and cooling at cloud top, which leads to destabilization and  
 83 in-cloud convective mixing (Dobbie & Jonas, 2001; Schmidt & Garrett, 2013). Solar heat-  
 84 ing of cloud top during the day works against this destabilization but is generally weaker  
 85 in magnitude than LW heating (Ackerman et al., 1988). Optically thin cirrus are heated  
 86 throughout by both LW and SW; this generates buoyancy and drives a mesoscale cir-  
 87 culation that lofts the cloud with respect to its clear-sky surroundings and promotes lat-  
 88 eral spreading (Dinh et al., 2010; Durran et al., 2009). The importance of radiatively driven

89 motions in the anvil cloud life cycle is supported by cloud-resolving model simulations  
 90 showing that anvil lifetimes are substantially prolonged by radiative heating (Dobbie &  
 91 Jonas, 2001; Hartmann et al., 2018; Gasparini et al., 2019). However, the relative im-  
 92 portance of in-cloud convection and mesoscale lofting remains unclear.

93 Recent work has helped to better understand the connections between radiative  
 94 heating, anvil cloud evolution, and the climatological NCRE of tropical convection. Hartmann  
 95 and Berry (2017) hypothesized that radiative heating plays a critical role in driving the  
 96 convective cloud population towards one that results in the observed near-neutral NCRE.  
 97 Their hypothesis, which we refer to as the selective cloud maintenance hypothesis, posits  
 98 that the LW heating dipole in optically thick anvil clouds acts to thin them until the ver-  
 99 tical gradient in cloud radiative heating is strong enough to incite in-cloud convection,  
 100 which maintains the cloud at an optical thickness corresponding to a positive NCRE.  
 101 This maintenance of positive-NCRE anvils balances the negative NCRE exhibited dur-  
 102 ing the earlier stages of the MCS life cycle. The selective cloud maintenance hypothe-  
 103 sis was further explored by Hartmann et al. (2018), who found that radiatively driven  
 104 turbulence maintains moderately thick anvil clouds by vertically recycling water vapor.  
 105 In-cloud updrafts promote ice growth by vapor deposition, drive new ice crystal nucle-  
 106 ation, and counteract sedimentation. The water vapor supply is then replenished by the  
 107 sublimation of ice crystals in descending air parcels. The strength of this “microphys-  
 108 ical cycling” mechanism is sensitive to changes in the model microphysical scheme, and  
 109 the importance of fresh ice crystal nucleation is particularly unclear. Other simulations  
 110 have found nucleation to play a lesser role in cloud maintenance (Gasparini et al., 2019),  
 111 and aircraft measurements of anvil clouds in the eastern Pacific found only a couple of  
 112 cases in which ice crystal concentrations were reflective of nucleation events (Jensen et  
 113 al., 2009).

114 The selective cloud maintenance hypothesis and microphysical cycling mechanism  
 115 have yet to be validated by observations. Previous observational studies have used geo-  
 116 stationary satellite measurements to track the radiative evolution of individual MCSs  
 117 (Wall et al., 2018) and spaceborne radar retrievals to examine anvil vertical structure  
 118 (Yuan et al., 2011). In both of these studies, instrumental limitations prevented the de-  
 119 tection of certain cloud properties that are important to the evaluation of anvil cloud  
 120 maintenance mechanisms. In situ observations (e.g., Heymsfield et al., 2002; Jensen et  
 121 al., 2009) have provided important insights into anvil cloud vertical structure but are lim-  
 122 ited in amount and scope.

123 The objective of this study is to characterize the microphysical and macrophysi-  
 124 cal evolution of tropical anvil clouds using the observational tools necessary to capture  
 125 their entire life cycle. In doing so, we evaluate the selective cloud maintenance hypothe-  
 126 sis, the relative importance SW and LW radiative heating, and the plausibility of mi-  
 127 crophysical cycling. In section 2, we describe the satellite data and methodologies that  
 128 are used to identify anvil clouds and deep convective cores, calculate radiative heating  
 129 rates, and examine anvil cloud evolution. Results are presented in section 3 and discussed  
 130 in section 4. We summarize our findings and discuss their implications in section 5.

## 131 2 Data and Methodology

132 In this section, we describe the data and methodologies used to identify anvil clouds  
 133 and deep convective cores. We then discuss how composites of thinning anvils are con-  
 134 structed and used to calculate radiative heating rates.

135 We use observations from several instruments aboard satellites belonging to the A-  
 136 train constellation (Stephens et al., 2002), which follows a sun-synchronous orbit that  
 137 crosses the equator at approximately 01:30 and 13:30 local time (which we also refer to  
 138 as night and day, respectively). This allows for the comparison of daytime and night-

139 time cloud populations but precludes the study of how individual anvil clouds evolve over  
 140 time. Geostationary satellite measurements have been used in the past to examine the  
 141 MCS life cycle (Wall et al., 2018), but these passive sensors fail to capture optically thin  
 142 anvil clouds and cannot provide information about vertical structure, both of which are  
 143 necessary to evaluate anvil maintenance processes. A-train observations are obtained for  
 144 the full 2009 calendar year apart from two periods for which data are unavailable (Feb.  
 145 16 to March 12 and Dec. 8 to 31).

146 We consider two tropical maritime regions extending from 12°S to 12°N: the In-  
 147 dian Ocean (IO; 55°E-95°E) and the West Pacific (WP; 150°E-180°E). These two re-  
 148 gions both have a small climatological NCRE despite frequent deep convection (Ramanathan  
 149 et al., 1989; Harrison et al., 1990), and MCSs in both regions tend to be aggregated into  
 150 large complexes consisting of several convective cores with connected anvil cloud decks  
 151 (Yuan & Houze, 2010). This stands in contrast to the nearby Maritime Continent re-  
 152 gion, in which MCSs are frequent and extensive but tend to be separated from one an-  
 153 other. In order to restrict our analysis to maritime convection, we exclude observations  
 154 from the southern tip of the Indian subcontinent that falls within the bounding box of  
 155 the IO region.

## 156 2.1 Anvil Clouds

### 157 2.1.1 Satellite Retrievals

158 A-train hosts the Cloud-Aerosol Lidar and Infrared Pathfinder Satellite Observa-  
 159 tions (CALIOP) instrument aboard the CALIPSO satellite and the Cloud Profiling Radar  
 160 (CPR) aboard the CloudSat satellite. Berry and Mace (2014) demonstrated that both  
 161 instruments are needed to detect the full spectrum of radiatively active cirrus in trop-  
 162 ical convective regions. The sensitivity of CALIOP to small ice crystals allows it to de-  
 163 tect thin cirrus clouds and the tenuous tops of thicker cloud layers. However, because  
 164 the lidar signal becomes fully attenuated at an optical depth of 4-5, it is unable to cap-  
 165 ture the full extent of optically thick clouds (Winker et al., 2010). Those clouds are bet-  
 166 ter captured by the CloudSat radar’s longer wavelength, which is sensitive to large ice  
 167 crystals but does not detect the smaller ones seen by CALIOP. The coincident radar and  
 168 lidar observations offered by the A-train constellation can thus be synergistically used  
 169 to detect cloudy volumes with a wide range of optical properties.

170 We obtain combined CloudSat-CALIPSO observations from two DARDAR (raDAR-  
 171 liDAR) data products. As described in Delanoë and Hogan (2008), the DARDAR algo-  
 172 rithm combines CALIOP and CPR measurements using a variational scheme that es-  
 173 timates ice cloud properties for cloudy volumes detected by both instruments and for  
 174 those detected by only one instrument. When both instrument are available, two inde-  
 175 pendent pieces of information are known about the cloud particle size distribution, which  
 176 allows the retrieval to rely less on empirical, a priori estimates than it does for regions  
 177 detected by only one instrument. The DARDAR grid has a vertical resolution of 60 m  
 178 and  $\sim 1.1$ -km horizontal spacing between profiles. More than 4.2 million profiles are used  
 179 in this study (57% from the IO region, 43% from the WP), which are about evenly split  
 180 between day and night.

181 Cloud layer information and ice microphysical properties are obtained from DARDAR-  
 182 CLOUD v2.1.1 (Delanoë & Hogan, 2010). DARDAR-CLOUD uses a vertical separation  
 183 threshold of 480 m to distinguish cloud layers and provides profiles of retrieved visible  
 184 extinction coefficient ( $\alpha_v$ ), ice water content (IWC), and effective radius ( $r_e$ ). We fur-  
 185 ther calculate the visible optical depth ( $\tau$ ) and IWP of each cloud layer by vertically in-  
 186 tegrating  $\alpha_v$  and IWC, respectively. DARDAR-CLOUD has been extensively used and  
 187 evaluated against in situ observations and other combined retrieval products (e.g., Deng  
 188 et al., 2013; Stein et al., 2011; Delanoë et al., 2013). Nevertheless, the errors associated  
 189 with the retrieval algorithm are substantial, especially in regions detected by only one

instrument, and several shortcomings in the DARDAR-CLOUD version used here have been identified. The most relevant shortcoming to this study is the apparent overestimation of  $\alpha_v$  and IWC in regions seen by the lidar alone (Deng et al., 2013), which implies that the cloud layer  $\tau$  and IWP calculated in the present study may be biased high in some cases. For a more detailed discussion of the errors associated with DARDAR-CLOUD and the improvements made to reduce them, we direct the reader to Delanoë and Hogan (2010) and Cazenave et al. (2019).

In addition to the DARDAR-CLOUD retrievals, we obtain estimates of ice crystal number concentration from DARDAR-Nice v1.0 (Sourdeval et al., 2018). We use the DARDAR-Nice retrieval of the concentration of ice crystals with a maximum diameter greater than  $5 \mu\text{m}$  ( $N_i$ ). The  $N_i$  estimation methodology assumes a monomodal particle size distribution, which may introduce bias at temperatures above  $-50^\circ\text{C}$ , since bimodal distributions become increasingly likely at warmer temperatures. We do not expect this to jeopardize the results of this study, which focuses primarily on  $N_i$  measurements at colder temperatures. Sourdeval et al. (2018) and Krämer et al. (2020) compared DARDAR-Nice to aircraft observations and found generally good agreement, but both noted that DARDAR-Nice overestimates  $N_i$  by a factor less than 2 for temperatures colder than  $-60^\circ\text{C}$ . While this may affect the quantitative accuracy of the anvil  $N_i$  reported here, it does not impact our qualitative conclusions.

### 2.1.2 Correcting for the Diurnal Cycle of Lidar Sensitivity

Because we seek to compare daytime (13:30 LT) and nighttime (01:30 LT) observations of anvil clouds, differences in instrument sensitivity during day and night must be taken into account. The CALIOP minimum detectable backscatter is highest during the day due to background solar noise (McGill et al., 2007), which prevents the detection of tenuous cloud features that would otherwise be detected at night. This difference can be seen in Figure 2, which shows daytime and nighttime histograms of DARDAR-CLOUD  $\alpha_v$  for pixels seen by the lidar only. The diurnal cycle of lidar sensitivity is apparent at low values of  $\alpha_v$ , which are detected frequently at 01:30 but rarely at 13:30. The histograms show much better agreement for values of  $\alpha_v$  exceeding the daytime modal value, which suggests a reduced impact of solar noise. Low- $\alpha_v$  pixels are often found at cloud edge, which complicates the comparison of 01:30 and 13:30 cloud geometries. To account for this, we remove all cloudy, lidar-only pixels from the DARDAR retrievals for which  $\alpha_v$  is less than  $0.12 \text{ km}^{-1}$  and treat them as if they are clear sky. The threshold corresponds to the daytime modal value and is indicated by the dashed black line in Figure 2. The correction removes 21.5% of daytime lidar-only pixels and 49.0% of nighttime lidar-only pixels, which has important implications for the detection of properties such as cloud top height and geometric thickness. On average, cloud layer top height is reduced by 126 and 333 m during day and night, respectively. Despite this, the impact of the correction on cloud layer  $\tau$  is negligible, since the affected pixels contribute relatively little to the layer-integrated  $\alpha_v$ . The implications of the correction on cloud fraction statistics are discussed in section 3.1.

### 2.1.3 Anvil Identification

For the purposes of this paper, we use the term “anvil cloud” to refer to high ice cloud layers that are likely produced by deep convection. After low- $\alpha_v$  pixels have been removed to correct for the diurnal bias in lidar sensitivity, we identify the uppermost four cloud layers in each profile using the DARDAR cloud layer index. A layer is classified as an anvil cloud if it meets the following three criteria:

1. The layer cloud top height (CTH) exceeds 10 km. This excludes mid-level convection from our analysis and corresponds to the minimum CTH used by Berry and Mace (2014) in their definition of cirrus layers.

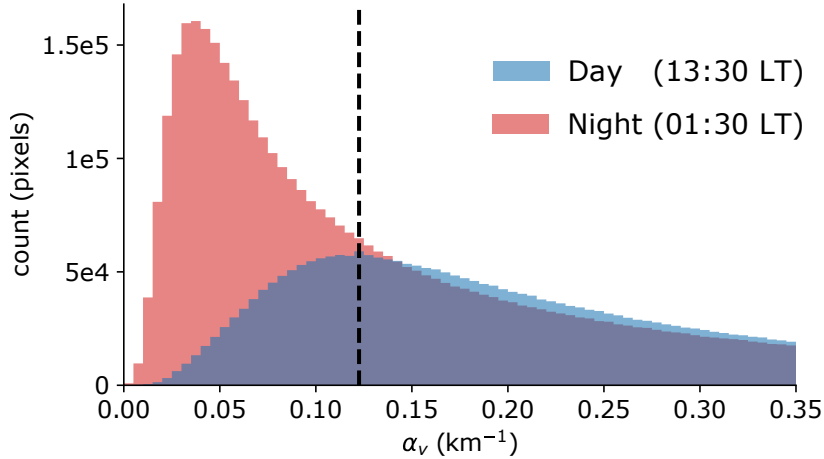


**Figure 2.** Histograms of visible extinction coefficient ( $\alpha_v$ ) for DARDAR-CLOUD lidar-only pixels during the (blue) 13:30 LT and (red) 01:30 LT equatorial crossings. The dashed line shows the threshold used to correct for the diurnal variation in lidar sensitivity. The histograms use data from the WP and IO study regions for the full month of May, 2009.

- 240 2. The layer cloud base height (CBH) exceeds 5 km, which corresponds to the av-
- 241 erage freezing level in the study regions as calculated from reanalysis temperature
- 242 included in DARDAR-CLOUD (originally from the European Centre for Medium-
- 243 Range Weather Forecasts). This criterion is intended to exclude deep convective
- 244 cores, which have bases near the surface.
- 245 3. The layer IWP exceeds  $10 \text{ g m}^{-2}$ . This threshold corresponds to the relative min-
- 246 imum between the two cirrus modes of the layer IWP distribution (Figure 1), and
- 247 we therefore expect that it carries physical meaning. Of course, it is possible that
- 248 some thin anvil layers are wrongly excluded by this criterion and that some thick
- 249 cirrus that are not of convective origin are wrongly included, but we expect these
- 250 cases to be small in number compared to our sample size.

251 Anvil layers found beneath non-anvil cirrus layers are included in our analysis but those

252 found beneath other anvils are not, so that no more than one anvil layer from each ver-

253 tical profile is included in our analysis.

254 The results of the anvil identification methodology for a typical scene are shown

255 in Figure 3a. This example demonstrates the ability of the three criteria to distinguish

256 cirrus layers connected to deep convection from thin cirrus of unknown origin, such as

257 the uppermost cloud layer present in the right-hand half of the scene. Limitations of our

258 methodology are also apparent. As an example, consider the lowermost cloud layer near

259  $7.5^\circ\text{S}$ , which is classified as an anvil cloud in some profiles but not in others. When the

260 vertical separation between this layer and the overlying one is less than 480 m, a single

261 anvil layer is identified that extends from  $\sim 7$  to  $\sim 15$  km. When the separation exceeds

262 480 m, two distinct layers are identified, and the lower one is excluded from analysis. Be-

263 cause our methodology considers each profile individually, it cannot account for nuances

264 such as these that are apparent when the profile is viewed within its larger context. We

265 have inspected more cloud scenes and found that scenarios such as the one discussed here

266 are rare, and we do not expect this limitation to have significant impacts on our results.

267 Figure 3b shows which portions of the cloud scene are detected by the CALIPSO

268 lidar and CloudSat radar and makes clear that both instruments are needed to accurately

269 determine CTH and geometric thickness. Some thin anvil layers (such as those on the  
 270 left-hand edge of the scene) would go entirely undetected if only radar observations were  
 271 used. Of all anvil layers identified in this study, 72.1% are detected by both instruments  
 272 (though not necessarily at the same altitude), 27.6% are detected by only the lidar, and  
 273 0.3% are detected by only the radar. This supports the conclusion of Berry and Mace  
 274 (2014) that both instruments are needed to capture the full spectrum of radiatively ac-  
 275 tive ice clouds. It is also evident in Figure 3b that the stretches of cloud seen by both  
 276 the radar and the lidar are quite limited; this has important implications for retrieval  
 277 uncertainty, for which we direct the reader to the aforementioned references.

## 278 2.2 Convective Cores

279 We use observations of 11- $\mu\text{m}$  brightness temperature ( $\text{TB}_{11}$ ) to identify deep con-  
 280 vective cores and find the spreading distance ( $d_{\text{core}}$ ) of each anvil observations from the  
 281 nearest core. Because the cloud-free atmosphere is nearly transparent to infrared radi-  
 282 ation in the 11- $\mu\text{m}$  band,  $\text{TB}_{11}$  measured from space is sensitive to the presence of deep  
 283 convective clouds with cold tops. Observations are provided by the Moderate Resolu-  
 284 tion Imaging Spectroradiometer (MODIS) Level 2 Cloud Product (Platnick et al., 2017).

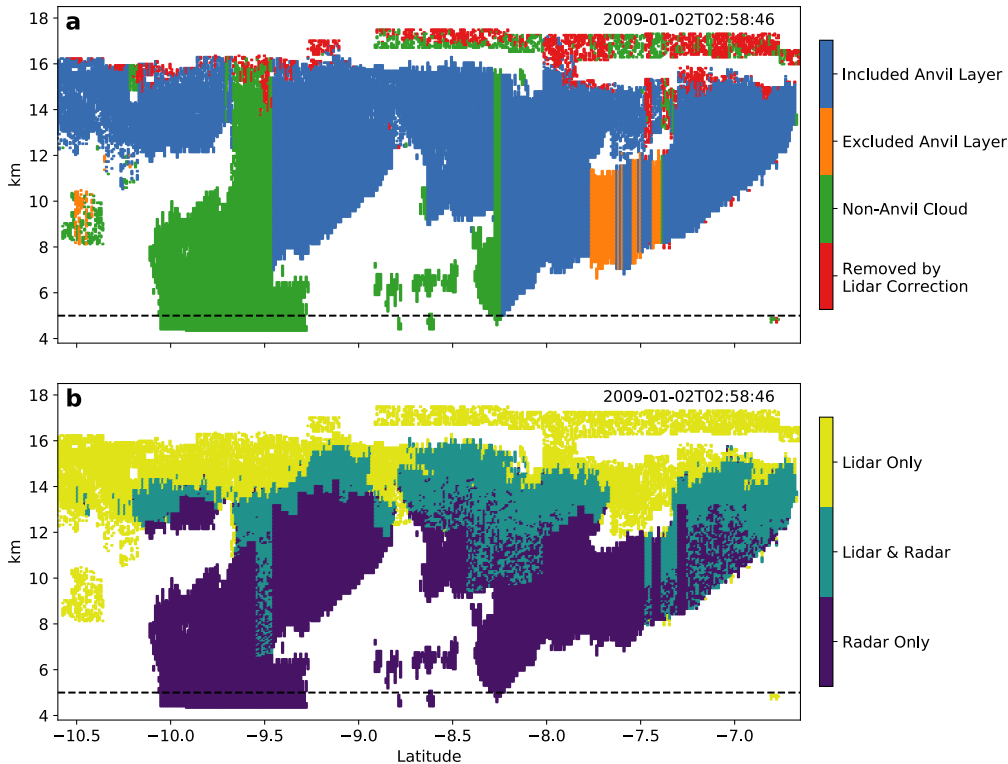


**Figure 3.** Example DARDAR-CLOUD scene from the West Pacific region. (a) Results of our anvil identification algorithm showing (blue) anvil cloud layers included in our analysis, (orange) anvil layers excluded from analysis because they are not the uppermost anvil layer in the column, (green) non-anvil layers, and (red) cloudy pixels that did not meet the minimum extinction threshold required by the lidar sensitivity correction. (b) Availability of lidar and radar measurements. The dashed black line at the 5-km level indicates the minimum cloud base height permitted for anvil layers.

285 MODIS is a scanning radiometer aboard the Aqua satellite that provides plan view TB<sub>11</sub>  
 286 observations (channel 31) coincident with CloudSat and CALIPSO measurements. Each  
 287 MODIS data granule has a swath width of 2,330 km and includes 5 minutes of obser-  
 288 vations, corresponding to an along-track length of about  $\sim 2,000$  km. TB<sub>11</sub> measurements  
 289 are provided at  $5 \times 5$  km resolution.

290 Different methods of convective core identification using infrared brightness tem-  
 291 peratures have been demonstrated and discussed in the literature (e.g., Gettelman et al.,  
 292 2002; Setvák et al., 2006; Young et al., 2012). Here, we use a simple TB<sub>11</sub> threshold of  
 293 210 K. Any contiguous cluster of two or more MODIS pixels with TB<sub>11</sub> below 210 K is  
 294 considered a convective core (pixels sharing a corner are contiguous). We calculate  $d_{core}$   
 295 as the distance between each DARDAR anvil observation and the nearest core found in  
 296 the colocated MODIS swath, even if the core lies outside of the study region boundaries,  
 297 which is the case for  $\sim 10\%$  of anvil observations within the study region. Values of  $d_{core}$   
 298 are invalid if they exceed the distance between the DARDAR profile and the nearest edge  
 299 of the MODIS swath. Since anvils may persist far from their convective source in both  
 300 space and time, we do not consider whether an anvil observation and its nearest core be-  
 301 long to the same contiguous cloudy region. The TB<sub>11</sub> at the location of the DARDAR  
 302 profile is also found using nearest-neighbor interpolation.

303 This method of convective core identification is susceptible to two types of errors.  
 304 First, as demonstrated in Young et al. (2012), optically thick anvil clouds can be mis-  
 305 takenly classified as convective core when a 210-K TB<sub>11</sub> threshold is used. This type  
 306 of error would increase the apparent size of a core by mistakenly including some of the  
 307 surrounding anvil, which would result in artificially low  $d_{core}$  values for the anvil obser-  
 308 vations associated with that core. Second, our method could fail to detect deep convective  
 309 towers that do not have sufficiently cold TB<sub>11</sub> signatures but nevertheless produce  
 310 anvil cloud. This type of error would result in inflated  $d_{core}$  values for anvils associated  
 311 with warmer cores. We inspected the  $d_{core}$  values assigned to anvil layers thicker than  
 312 the 95th percentile of geometric thickness (7.74 km), which are likely to be freshly de-  
 313 trained and close to their convective source. Approximately one fourth of these anvil pro-  
 314 files are found to have  $d_{core}$  exceeding 100 km. This suggests that a non-negligible amount  
 315 of convective cores may go undetected by a 210-K threshold, which is consistent with  
 316 previous findings (Young et al., 2012).

317 While this convective core identification methodology is relatively crude, it is suf-  
 318 ficient for our purposes. In this study, we use  $d_{core}$  mainly to show that anvil clouds can  
 319 routinely be found far away from a convective source. Errors in  $d_{core}$  values on the or-  
 320 der of tens of kilometers are inconsequential for these purposes, since MCSs can extend  
 321 horizontally for hundreds of kilometers. Detailed analyses of MCS structure require a  
 322 more precise method of core identification such as those used by Yuan and Houze (2010)  
 323 and Igel et al. (2014).

### 324 2.3 Anvil Cloud Composites and Radiative Heating

325 The cloud observations from A-train satellites are instantaneous snapshots, which  
 326 precludes us from examining how anvil clouds evolve over time. Instead, we composite  
 327 the anvil cloud profiles using  $\tau$  as the basis, since it is tightly linked to cloud radiative  
 328 heating and the hypotheses we seek to evaluate. To generate composites of thinning anvils,  
 329 each observation is first assigned to one of four groups based on region (WP or IO) and  
 330 time of day (01:30 or 13:30). The anvil profiles within each group are binned by  $\log_{10}\tau$   
 331 using a bin width of 0.1, and statistics are obtained for each bin.

332 Anvil  $\tau$  generally decreases with time after detrainment due to horizontal spread-  
 333 ing, precipitation, and ice crystal sedimentation. However, because the initial  $\tau$  of freshly  
 334 detrained anvils likely varies from storm to storm, it is possible that a particular anvil  
 335 was detrained more recently than an optically thicker one detected at the same moment

336 in time. Furthermore, the typical lifetime of convectively generated cirrus can regularly  
 337 exceed the 12 hours between the two daily A-train overpasses (Luo & Rossow, 2004; Mace  
 338 et al., 2006). It is then likely that many of the aged, optically thin cirrus detected at  
 339 13:30 were detrained during the preceding night, and vice versa. For these reasons, it  
 340 should be remembered that the composites presented here simply reflect the anvil pop-  
 341 ulation at the time of the two A-train overpasses and are not necessarily representative  
 342 of how individual cloud systems evolve over time.

343 To calculate realistic cloud radiative heating rates, we must first construct profiles  
 344 of IWC and  $r_e$  that are representative of the anvil clouds in each  $\tau$  bin and retain their  
 345 vertical structure. Because the anvil ice particle size distribution varies vertically in a  
 346 characteristic way (Yuan et al., 2011; Heymsfield et al., 2002), we cannot simply aver-  
 347 age together the microphysics profiles from cloud layers at different altitudes and tem-  
 348 peratures, since this would smear out much of the vertical structure. Instead, we gener-  
 349 ate IWC and  $r_e$  profiles using the following procedure. Within each  $\tau$  bin, we select  
 350 anvil profiles that have CTH within 500 m of the  $\tau$ -bin median, calculate the median CBH  
 351 of that subset, and keep only those profiles with CBH within 500 m of that. We then  
 352 find the median IWC and  $r_e$  of the remaining profiles at each vertical level and inter-  
 353 polate onto the 500-m vertical grid used in the radiative heating model. The resulting  
 354 profiles have retained the altitude, geometric thickness, and microphysical structure char-  
 355 istic of observed anvil clouds with similar  $\tau$ .

356 The IWC and  $r_e$  profiles for each  $\tau$  bin are fed into the single-column rapid radiative  
 357 transfer model for general circulation modeling (RRTMG; Mlawer et al., 1997; Iacono  
 358 et al., 2000). We use a surface temperature of 28 °C and albedo of 0.08, 400 ppm  
 359 CO<sub>2</sub>, and average temperature, water vapor, and ozone profiles for the study region as  
 360 calculated from 1989-2007 ERA-Interim reanalysis. For the 13:30 anvil profiles, we use  
 361 insolation corresponding to 13:30 LT on the equinox (1,261 W m<sup>-2</sup>). Ice cloud treatment  
 362 follows Fu (1996) and Fu et al. (1998). Recent work has shown that cirrus cloud radiative  
 363 forcing can be underestimated by radiative transfer algorithms that do not account  
 364 for ice crystal surface complexity (Järvinen et al., 2018). Cirrus optical properties are  
 365 also sensitive to assumptions about ice crystal habit (Wendisch et al., 2007). Detailed  
 366 treatment of these issues is important for modeling the role of cirrus in global climate,  
 367 but is beyond the scope of this study.

Radiative heating model output is used to calculate the net heating rate,  $Q_R$ , which  
 is equal to the sum of the SW and LW heating rates for the 13:30 observations and sim-  
 ply equal to the LW heating rate for the 01:30 observations. From this, we calculate the  
 mass-averaged net heating rate for the cloud layer,  $\bar{Q}_R$ , which can help understand the  
 potential for mesoscale anvil lofting. We also calculate the mass-averaged, in-cloud lapse  
 rate tendency (LRT) due to radiative heating:

$$\left. \frac{\partial \Gamma}{\partial t} \right|_{rad} = - \frac{1}{P_B - P_T} \int_{P_T}^{P_B} \frac{\partial Q_R}{\partial z} dP \quad (1)$$

368 where  $\Gamma$  is the lapse rate, and  $P_B$  and  $P_T$  are the pressures at cloud base and top, re-  
 369 spectively. The LRT is a measure of the destabilization produced by a vertically vary-  
 370 ing  $Q_R$ . If there is stronger heating at cloud base than at cloud top ( $\partial Q_R / \partial z < 0$ ), the  
 371 vertical column is destabilized and the LRT is positive. On the contrary, if heating is stronger  
 372 at cloud top ( $\partial Q_R / \partial z > 0$ ), the column is stabilized and the LRT is negative.

## 373 2.4 Statistical Analysis

374 The procedure described up to this point generates four composites (one for each  
 375 unique combination of study region and time of day) and a single profile of ice micro-  
 376 physics and radiative heating for each  $\tau$  bin within the composites. While these profiles  
 377 are realistic, they cannot capture the diversity of structures found among the  $\sim 1.35$  mil-

378 lion anvil profiles used in this study, and they do not provide a basis for statistical eval-  
 379 uation. To bolster the statistical robustness of our results, we randomly split each of the  
 380 four groups of anvil profiles into 100 subsamples and repeat the compositing procedure  
 381 and radiative heating calculations for each. The subsample sizes are equal within each  
 382 of the four groups of observations but vary between the groups from 3,105 for the WP  
 383 at 01:30 to 3,763 for the IO at 13:30. This resampling provides us with 100 independent  
 384 microphysical and radiative heating profiles for each unique combination of  $\tau$ , study re-  
 385 gion, and time of day. Composites shown in section 3 reflect the average of the 100 sub-  
 386 sample composites within each group. The subsample composites are also used to test  
 387 for significant differences in cloud properties between the 01:30 and 13:30 observations  
 388 using the nonparameteric Mann-Whitney-Wilcoxon test with a two-tailed significance  
 389 level of  $\alpha = 0.01$ . While the subsampling and large initial sample size used in this study  
 390 provide a high level of statistical confidence, it is important to remember that our re-  
 391 sults remain susceptible to any biases in the DARDAR retrievals.

### 392 **3 Results**

393 We begin by discussing the results of our anvil cloud identification scheme in sec-  
 394 tion 3.1. We then examine the distribution of anvil  $\tau$  (section 3.2) and its evolution with  
 395 spreading distance (section 3.3). In sections 3.4, 3.5, and 3.6, we discuss anvil macro-  
 396 physical structure, radiative heating, and microphysical structure, respectively.

#### 397 **3.1 Anvil Cloud Detection**

398 The results of our anvil cloud identification process are provided by region and time  
 399 of day in Table 1. Altogether, anvil cloud layers are identified in 32.1% of retrieval pro-  
 400 files. This is higher than that reported by Yuan and Houze (2010), who used a  $TB_{11}$  thresh-  
 401 old of 260 K to identify high cloud complexes (which include anvils). We find that 56.0%  
 402 of the anvil profiles identified here have interpolated MODIS  $TB_{11}$  greater than 260 K,  
 403 which can explain the difference between results. This shows that many anvil clouds are  
 404 sufficiently transparent to LW radiation to avoid detection by  $TB_{11}$  thresholds and has  
 405 important implications for observational studies of convective cloud populations.

406 Anvils account for about one half of all cloud layers with tops above 10 km and bases  
 407 above 5 km, which is consistent with previous findings that approximately half of the  
 408 cirrus clouds in tropical convective regions are associated with deep convection (Massie  
 409 et al., 2002; Luo & Rossow, 2004; Mace et al., 2006). We note, however, that the statis-  
 410 tics in Table 1 were computed after the lidar bias correction described in section 2.1.2  
 411 was applied. Without the bias correction, the overall anvil cloud fraction would be only  
 412 0.8% higher but the total cloud fraction would be 8.4% higher. This results in a slightly  
 413 lower ratio of anvil cirrus to total cirrus but is still in line with previous findings. The  
 414 difference indicates that the bias correction completely erases a substantial amount of  
 415 thin, non-anvil cirrus and may not be suitable for studies of thin cirrus climatology.

416 Table 1 also provides information about the vertical columns in which anvil cloud  
 417 layers were detected. The majority of anvil-containing profiles (84.7%) contain a single  
 418 anvil layer that is the uppermost cloud layer in the profile. The remainder contained mul-  
 419 tiple cloud layers meeting the anvil requirements (3.4%), a non-anvil layer located above  
 420 the anvil (11.9%), or both (0.2%). The presence of thin cirrus clouds above thicker anvil  
 421 cirrus has been previously observed and discussed (e.g. Winker & Trepte, 1998; McFar-  
 422 quhar et al., 1999). We find overlying cirrus to be more common during the day (15.0%  
 423 of anvil-containing profiles) than at night (8.6%) and more common in the WP (14.3%)  
 424 than in the IO (9.7%). Overlying cirrus are optically and geometrically thin, and have  
 425 a median CTH of 16.0 and 15.5 km in the WP and IO, respectively. We note that these  
 426 statistics only pertain to overlying cirrus containing at least one pixel with  $\alpha_v$  exceed-  
 427 ing the threshold used for the lidar diurnal bias correction. The frequency of overlying

**Table 1.** Anvil cloud identification results

	All	Day <sup>a</sup>	Night <sup>b</sup>	West Pacific	Indian Ocean
Number of profiles	4,239,774	2,119,485	2,120,641	1,808,562	2,431,212
Total Cloud Fraction	63.1%	63.4%	62.8%	71.4%	56.9%
Anvil Cloud Fraction	32.1%	33.0%	31.2%	35.0%	29.9%
<b>Fraction of anvil cloud profiles with:</b>					
Single anvil layer (no overlying cirrus)	84.7%	80.7%	88.8%	81.8%	87.2%
Multiple anvil layers (no overlying cirrus)	3.2%	4.0%	2.3%	3.5%	2.9%
Single anvil layer with overlying cirrus	11.7%	14.7%	8.5%	14.0%	9.6%
Multiple anvil layers with overlying cirrus	0.2%	0.3%	0.1%	0.3%	0.1%
<b>Median properties of overlying non-anvil cirrus:</b>					
Cloud top height (km)	15.8	15.8	15.8	16.0	15.5
Thickness (km)	0.60	0.66	0.54	0.60	0.60
Optical thickness	0.12	0.12	0.11	0.11	0.12

*Note.* All values are calculated from DARDAR-CLOUD after the removal of low-extinction pixels as described in section 2.1.2.

<sup>a</sup>data from the 13:30 LT A-train equatorial overpass. <sup>b</sup>data from the 01:30 LT overpass.

428 cirrus reported here should therefore be interpreted as a lower bound, and the geomet-  
429 ric and optical properties do not reflect the thinnest cirrus.

### 430 3.2 Anvil Optical Thickness

431 Figure 4 shows the distributions of anvil  $\tau$  and IWP observed at 13:30 and 01:30.  
432 They are normalized by dividing the number of observations in each bin by the total num-  
433 ber of retrieval profiles at 13:30 or 01:30 so that they essentially represent anvil cloud  
434 fraction as a function of IWP and  $\tau$ . The colored shading indicates the standard devi-  
435 ation of the 100 independent subsample histograms. The subsamples show very good agree-  
436 ment, indicating that the distribution shape is statistically robust. There are no major  
437 differences between the WP and IO distributions (not shown).

438 During both times of day, the IWP distribution peaks at  $\sim 28 \text{ g m}^{-2}$ , which matches  
439 the convective outflow peak in Figure 1 and approximately corresponds to the IWP at  
440 which high ice cloud layers exert their maximum NCRE (Berry & Mace, 2014; Hartmann  
441 & Berry, 2017). As expected, the distributions of anvil  $\tau$  closely resemble those of IWP  
442 and have peaks at  $\sim 1.4$ . The frequency of anvils with  $\tau < 0.8$  (grey shading in Figure  
443 4b) is artificially reduced due to our requirement that anvil clouds have an IWP greater  
444 than  $10 \text{ g m}^{-2}$ . The peak at 1.4, however, is not an artifact of our anvil identification  
445 methodology (see Text S1 and Figures S1-S3). We note that while 0.3% of anvil pro-  
446 files have  $\tau$  exceeding 40, the figures in this paper only show results for  $\tau < 40$  so that  
447 details are visible.

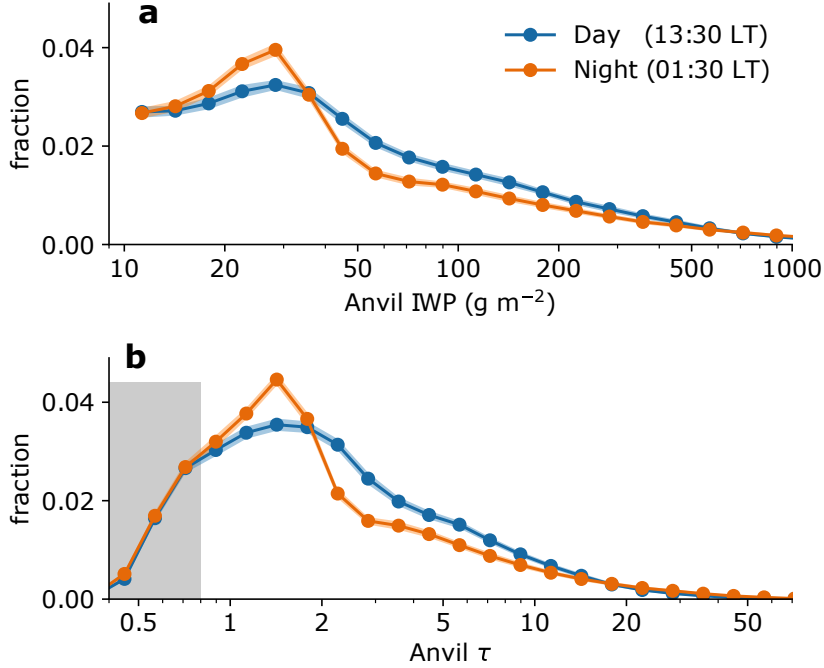


**Figure 4.** Anvil cloud fraction as a function of anvil (a) IWP and (b)  $\tau$  at 13:30 (blue) and 01:30 (orange). Colored shading indicates the standard deviation of histograms generated by randomly splitting the data into 100 subsamples of equal size. In (b), the grey shading indicates the  $\tau$  interval where the anvil fraction is artificially low due to the use of an IWP threshold of  $10 \text{ g m}^{-2}$  during anvil identification. Measurements are combined from the WP and IO regions. IWP and  $\tau$  bin widths are 0.1 in log space.

448 The anvil IWP and  $\tau$  distributions show important diurnal differences. First, the  
 449 01:30 distribution contains fewer optically thick clouds with IWP between 40 and 600  
 450  $\text{g m}^{-2}$  ( $2 \lesssim \tau \lesssim 20$ ) than the 13:30 distribution. Assuming that anvil IWP and  $\tau$  de-  
 451 crease over time, this suggests that the anvil population at 01:30 is, on the whole, more  
 452 aged than that at 13:30. This is consistent with the timing of the A-train equatorial cross-  
 453 ings in relation to the diurnal cycle of deep convective activity over oceans, which has  
 454 a maximum between 05:00 and 07:00 LT and a minimum in the evening hours (Nesbitt  
 455 & Zipser, 2003). The 13:30 A-train overpass takes place about 7 hours after the peak  
 456 in convective activity and would therefore encounter a “fresher” anvil cloud population  
 457 that the 01:30 overpass, which occurs 19 hours after the peak. Second, anvils with an  
 458 IWP between 20 and  $35 \text{ g m}^{-2}$  ( $1 \lesssim \tau \lesssim 2$ ) are more common at 01:30, but those with  
 459 an even lower IWP ( $10\text{-}20 \text{ g m}^{-2}$ ) are found at a similar frequency at both times of day.  
 460 As a result, the distribution peak is more pronounced at 01:30 than at 13:30. This sug-  
 461 gests that anvil clouds progress towards an optical depth of 1-2 over time but do not con-  
 462 tinue to thin as rapidly after that. We hereinafter refer to anvil clouds with  $\tau$  between  
 463 1 and 2 as “modal anvils.”

### 464 3.3 Anvil Spreading Distance

465 The distribution of anvil  $d_{core}$  across both study regions and times of day is shown  
 466 in Figure 5a. The large number of anvil profiles in the lowest  $d_{core}$  bin reflects the mis-  
 467 classification of optically thick anvils with  $TB_{11}$  below 210 K as convective cores. Other

468 than this, frequency initially increases with  $d_{core}$ , which is to be expected from the ver-  
 469 tical thinning and horizontal spreading of anvil clouds as they drift radially outwards from  
 470 the core into a stably stratified environment (Lilly, 1988). There is a peak between 30  
 471 and 60 km, but the location of the peak is sensitive to the  $TB_{11}$  threshold used for core  
 472 identification. Frequency decays exponentially beyond the peak, and approximately one  
 473 third of anvil profiles are located further than 250 km from the nearest core.

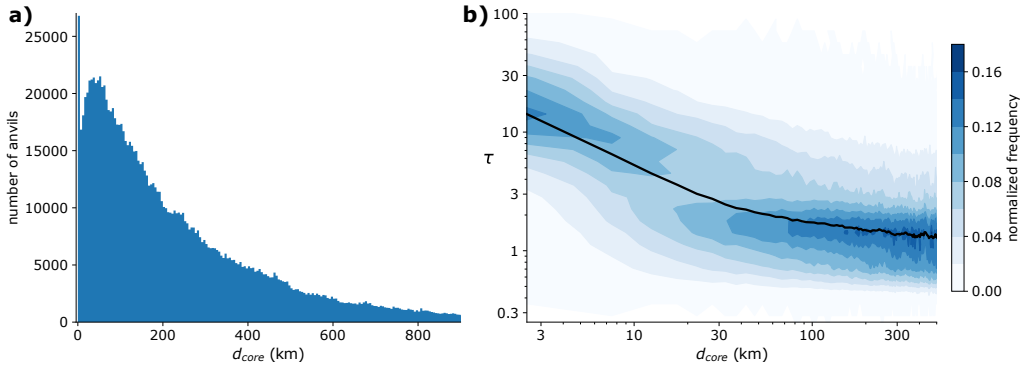


**Figure 5.** (a) Histogram of anvil cloud spreading distance,  $d_{core}$ . (b) Joint histogram of anvil  $d_{core}$  and  $\tau$ , with frequency normalized by column so that the values in each  $d_{core}$  bin add up to one. The black line indicates the median  $\tau$  for each  $d_{core}$  bin. Note that both axes use a linear scale in (a) but a logarithmic scale in (b). Bin widths are 5 km for  $d_{core}$  and 0.1 in log space for  $\tau$ .

474 The evolution of anvil  $\tau$  with spreading distance can be seen in Figure 5b, which  
 475 shows a joint histogram of  $\tau$  and  $d_{core}$  normalized so that the sum of frequencies in each  
 476  $d_{core}$  bin is equal to one. The black line indicates the median  $\tau$  of the clouds in each  $d_{core}$   
 477 bin. Freshly detrained anvils have a median  $\tau$  between 10 and 20 and are optically thicker  
 478 at 01:30 than at 13:30 (Figure S4). As anvils thin, median  $\tau$  follows two distinct power-  
 479 law decay regimes. Initially,  $\tau$  decays rapidly within 40 km of the convective core, which  
 480 coincides with the horizontal spreading indicated by Figure 5a and may be hastened by  
 481 anvil precipitation. This initial decay proceeds more rapidly at night (Figure S4). There  
 482 is then a transition to a slower decay regime which dominates between 50 and  $\sim 400$  km  
 483 of the core. Modal anvils increasingly dominate the population over this interval and con-  
 484 tinue to do so beyond 500 km (not shown).

485 So far, we have shown that there is a prevalence of anvil clouds with  $\tau$  between 1  
 486 and 2 at both 13:30 and 01:30 and that these modal anvils are uniquely capable or per-  
 487 sisting several hundred kilometers away from the nearest convective core. Together, these  
 488 two findings support the hypothesis that anvils are driven towards and maintained at  
 489 an optical thickness corresponding to a positive NCRE. They do not, however, provide  
 490 insight into the mechanisms responsible for cloud maintenance. To examine those, we  
 491 turn to the composites of anvil cloud macrophysical, radiative, and microphysical prop-  
 492 erties.

### 493 3.4 Macrophysical Structure

494 Changes in CTH and geometric thickness (calculated here as CTH–CBH) can pro-  
 495 vide further insight into the processes responsible for anvil cloud evolution and main-  
 496 tenance. The evolution of these properties with respect to  $\tau$  is shown in Figure 6. The  
 497 contour plots show the fraction of profiles in each  $\tau$  bin that contain anvil cloud at a given

498 height and thus reflect the typical height and thickness of anvils at different stages of op-  
 499 tical thinning. Black lines indicate median CTH and CBH. Median geometric thickness  
 500 is shown below the corresponding cloud fraction composites (shading shows one stan-  
 501 dard deviation). The diurnal difference in geometric thickness is statistically significant  
 502 ( $\alpha = 0.01$ ) everywhere except for  $\tau \approx 6$  and  $\tau \gtrsim 30$  in the IO. Anvil cloud evolution  
 503 and its diurnal differences are more pronounced in the WP than in the IO but are qual-  
 504 itatively similar in both regions; for the sake of simplicity, any numeric values referenced  
 505 in our discussion are for the WP.

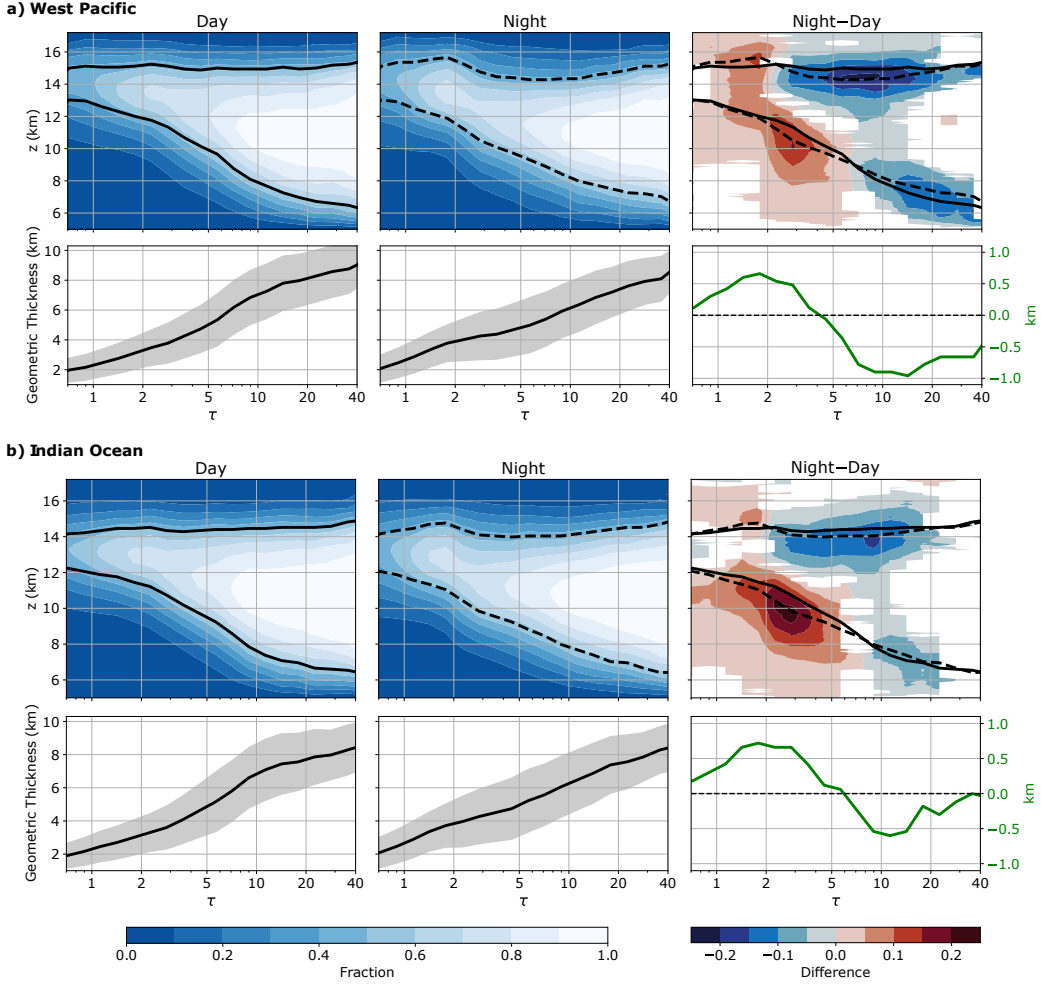


**Figure 6.** Anvil cloud geometry as a function of  $\tau$  in the (a) West Pacific and (b) Indian Ocean regions, shown for (left) day, (middle) night, and (right) night minus day. For each region and time of day, the top plot shows the fraction of anvil cloud profiles in each  $\tau$  bin that contain cloud at a given height. Black lines (solid for day, dashed for night) show median CTH and CBH. The bottom plots show median geometric thickness, with shading indicating one standard deviation. The green lines shows the difference in median geometric thickness between night and day and are plotted with a different vertical axis.

506 We begin with freshly detrained anvils. The optically thickest anvils are detrained  
 507 with similar CTH during day and night. Geometric thickness is typically between 6 and  
 508 9 km and is slightly greater at 13:30 due to the lower CBH found then. At night, cloud

509 top sinks nearly one kilometer and cloud base rises as  $\tau$  decreases from 40 to 10. This  
 510 results in rapid geometric thinning and is consistent with the flattening of convective out-  
 511 flow by positive buoyancy at cloud base and negative buoyancy at cloud top (Lilly, 1988).  
 512 During the day, the post-detrainment drop in CTH is small compared to that at night,  
 513 but the rise in CBH is similar. Geometric thinning is slower as a result, and daytime anvils  
 514 are nearly 1 km thicker than nighttime anvils by  $\tau \approx 10$ . As  $\tau$  decreases from 10 to 4,  
 515 CTH is relatively constant at both times of day and is  $\sim 600$  m lower at 01:30 than at  
 516 13:30. Geometric thinning over this interval is thus caused by the continued rise of cloud  
 517 base, which is greater during the day than at night. By  $\tau \approx 4$ , thickness is again sim-  
 518 ilar at both times of day, and nighttime anvils remain at a slightly lower altitude.

519 Several interesting macrophysical shifts occur as  $\tau$  approaches the modal range of  
 520 1-2. At night, median CTH in the WP rises by 1.2 km as  $\tau$  decreases from 4 to 1.8, where  
 521 it reaches its peak value (15.7 km). This rise in CTH is nearly as large as the rise in CBH  
 522 over the same interval, which results in very little geometric thinning. During the day,  
 523 the rise in median CTH is more modest ( $\sim 300$  m to a peak value of 15.2 km at  $\tau \approx 2.2$ )  
 524 and there is more geometric thinning. As a result, modal anvils observed during the day  
 525 are  $\sim 600$  m thinner and have a median CTH that is  $\sim 500$  m lower than their counter-  
 526 parts observed at night. There is also less variability in their geometric thickness: the in-  
 527 terquartile range is 1,380 m at 13:30 compared to 1,620 m at 01:30.

528 It is clear from Figure 6 that the macrophysical evolution of anvil clouds differs sub-  
 529 stantially between night and day despite similar initial conditions. At night, anvil tops  
 530 sink after detrainment, but modal anvils are found at high altitudes. Daytime CTH is  
 531 much more constant but nevertheless reaches its maximum as  $\tau$  approaches the modal  
 532 range. In the next section, we examine these diurnal differences in the context of radia-  
 533 tive heating.

### 534 3.5 Radiative Heating

535 Net radiative heating rates ( $Q_R$ ) are shown in Figure 7 and are provided as the mean  
 536 of the 100 subsample composites for each region and time of day. The spread in  $Q_R$  among  
 537 the subsample composites (Figure S5) is greatest at large  $\tau$  near cloud base and top, where  
 538 the magnitude of  $Q_R$  is generally largest and a difference in CTH or CBH of one ver-  
 539 tical level can have a large impact on  $Q_R$  at a fixed height. The diurnal difference in  $Q_R$ ,  
 540 shown in the third column of Figure 7, is statistically significant throughout most of the  
 541 composite. This is to be expected from the addition of SW heating during the day, but  
 542 we note that the diurnal difference in LW heating rates (not shown) is also statistically  
 543 significant throughout much of the composite. Figure 7 also shows the 100-subsample  
 544 mean LRT and  $\overline{Q_R}$ , with shading indicating the 100-subsample standard deviation. The  
 545 subsamples show good agreement with respect to  $\overline{Q_R}$  despite the substantial spread in  
 546  $Q_R$  at any fixed point in the composite. There is also good agreement for LRT, which  
 547 shows the largest spread at night for thick clouds undergoing strong cooling at cloud top  
 548 and heating at cloud base.

549 Upon detrainment, optically thick anvils undergo strong LW cooling at cloud top  
 550 of up to  $20 \text{ K day}^{-1}$ , which contributes to the negative buoyancy at the top of the out-  
 551 flow plume. During the day, SW heating cancels out much of this cooling, resulting in  
 552 a small  $Q_R$ . This 15-K diurnal difference in cloud-top  $Q_R$  helps explain why CTH de-  
 553 creases after detrainment at 01:30 but is maintained aloft at 13:30 and suggests that ra-  
 554 diative heating plays an important role in the early stages of the anvil life cycle. Dur-  
 555 ing both times of day, cloud base experiences strong LW heating. While this may con-  
 556 tribute to cloud base lofting, prior work has shown that the total diabatic heating near  
 557 the base of freshly detrained anvils is likely dominated by evaporative cooling (Gasparini  
 558 et al., 2019).

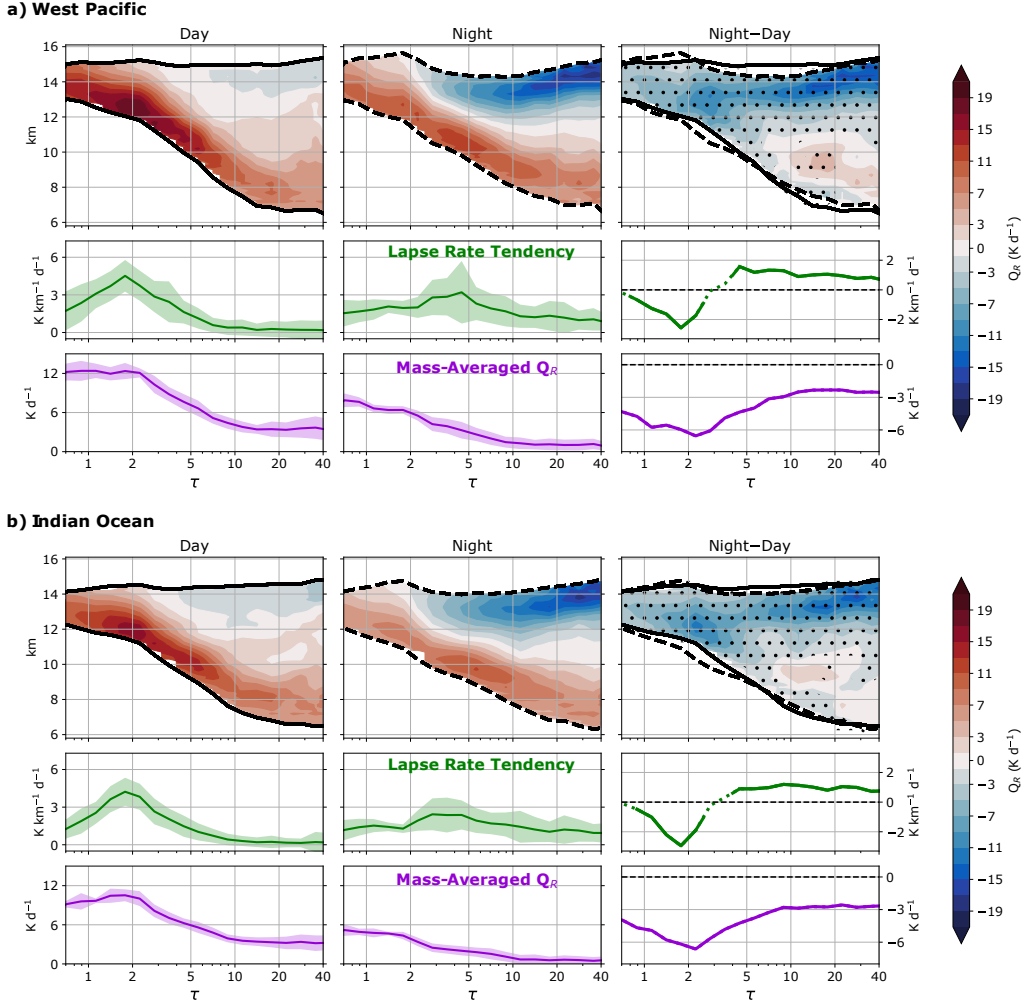


**Figure 7.** Net radiative heating rates for the (a) West Pacific and (b) Indian Ocean regions for (left) day, (middle) night, and (right) night minus day. For each region and time of day, the top plot shows the mean net heating rate of the 100 subsample composites. Stippling indicates a statistically significant diurnal difference ( $\alpha=0.01$ ), and black lines (solid for day, dashed for night) show median CTH and CBH. The middle and bottom rows show the 100-subsample mean lapse rate tendency (LRT) and mass-averaged layer heating ( $\overline{Q}_R$ ), respectively. Shading indicates the standard deviation of the subsample composites. The lines showing night–day LRT are solid where the difference is statistically significant and dotted otherwise. The night–day  $\overline{Q}_R$  is statistically significant at all  $\tau$ .

559 As  $\tau$  decreases from 10 to 4 and CBH continues to rise, the temperature difference  
 560 between cloud base and the surface increases. This strengthens LW heating at cloud base  
 561 and drives a gradual rise in  $\overline{Q}_R$  during both times of day. At night, the warming region  
 562 near cloud base and the cooling region near cloud top are brought closer together as the  
 563 cloud thins, which generates stronger heating gradients and causes LRT to increase. The  
 564 strongest destabilization (highest LRT) occurs at  $\tau \approx 4$ , when cloud base heating reaches  
 565 its maximum value and there is still substantial cooling near cloud top. During the day,  
 566 net heating at cloud top remains small as  $\tau$  decreases from 10 to 4, but  $\overline{Q}_R$  and LRT con-

567 continue to increase gradually. At  $\tau \approx 4$ , the contributions of SW and LW heating to total  
 568  $\overline{Q}_R$  are approximately equal, and  $\overline{Q}_R$  is nearly twice as strong as it is at night.

569 The heating characteristics of modal anvils are notable for several reasons. As  $\tau$   
 570 drops to 2, LW cooling at cloud top ceases, at which point the anvils are heated in their  
 571 entirety. As a result, modal anvils undergo stronger mass-averaged heating than their  
 572 optically thicker precursors, which is demonstrated by a substantial increase in  $\overline{Q}_R$ . This  
 573 coincides with the large increase in nighttime CTH. Furthermore, modal anvils show large,  
 574 statistically significant diurnal differences in both  $\overline{Q}_R$  and LRT. We examine each in turn.

575 The mass-averaged heating of modal anvils is nearly twice as high during the day  
 576 than at night. There are two reasons for this difference. First and most importantly is  
 577 SW heating, which accounts for about one third of total  $\overline{Q}_R$  during the day and  $\sim 75\%$   
 578 of the diurnal difference. The second reason, which accounts for the remaining 25%, is  
 579 the diurnal difference in modal anvil geometry. Because modal anvils at 13:30 are ge-  
 580 ometrically thinner than those at 01:30 but have equal  $\tau$ , they must have a higher in-  
 581 cloud  $\alpha_v$  on average. The higher  $\alpha_v$  results in greater LW flux convergence near cloud  
 582 base and thus stronger radiative heating there. In fact, the heating at modal anvil base  
 583 at 13:30 is the strongest heating found anywhere. Because of this geometric effect, mass-  
 584 averaged LW heating is greater during the day than at night (8.2 vs. 6.2 K day<sup>-1</sup> at  $\tau =$   
 585 1.8).

586 Modal anvils also undergo stronger radiative destabilization during the day. This  
 587 is unexpected, since SW heating is generally strongest near cloud top and therefore acts  
 588 to decrease LRT and stabilize the cloud. Again, cloud geometry is responsible for the  
 589 diurnal difference. Destabilization is driven by LW heating, which is highest near cloud  
 590 base and decreases with height. The geometric effect described in the previous paragraph  
 591 produces especially strong vertical gradients in LW heating during the day, which acts  
 592 to increase LRT. The LW LRT exceeds 4 K km<sup>-1</sup> day<sup>-1</sup>, which greatly outweighs the  
 593 stabilization provided by SW heating ( $-0.4$  K km<sup>-1</sup> day<sup>-1</sup>). Because of the geometric  
 594 effect, LRT at  $\tau = 1.8$  is twice as high during the day than at night, and the daytime  
 595 peak LRT exceeds the nighttime peak at  $\tau \approx 4$  by more than 40%.

596 In this section, we have shown that radiative heating hastens initial anvil thinning  
 597 at night but hinders it during the day. As anvils evolve, they are increasingly heated and  
 598 destabilized by LW radiation. Modal anvils are too tenuous to undergo LW cooling at  
 599 cloud top but still undergo substantial heating; as a result, their  $Q_R$  is higher than that  
 600 of their optically thick precursors. During the day, the thinner geometry of modal anvils  
 601 makes them more susceptible to LW heating and destabilization. Evidence of destabi-  
 602 lization may also be apparent in anvil microphysical structure, which is discussed in the  
 603 next section.

### 604 3.6 Microphysical Structure

605 The evolution of anvil microphysical structure can provide further insight into anvil  
 606 maintenance mechanisms. Figures 8 and 9 show 100-subsample mean composites of  $r_e$ ,  
 607  $N_i$ , and IWC. The 100 subsamples show good agreement when it comes to the median  
 608  $r_e$ ,  $N_i$ , and IWC at any particular point in the composite, but we note that there is sub-  
 609 stantial variability among the individual anvil profiles within each subsample (Figures  
 610 S6 and S7). Nevertheless, the anvil cloud vertical structure found here is consistent with  
 611 in situ aircraft measurements (McFarquhar & Heymsfield, 1996; Heymsfield et al., 2002;  
 612 Jensen et al., 2009; Lawson et al., 2010) and satellite observations (Yuan et al., 2011).  
 613 Median  $r_e$  generally decreases with altitude, as expected from gravitational size sorting  
 614 and the temperature dependence of ice diffusional growth.  $N_i$ , which is dominated by  
 615 smaller ice crystals, generally increases with height until its maximum  $\sim 1$  km below cloud  
 616 top. Despite high  $N_i$  near cloud top, maximum IWC is typically found 1-2 km above cloud  
 617 base and decreases with altitude above that point, suggesting that total IWC is dom-

618 inated by large ice crystals. The layer of low IWC at cloud base, sometimes accompa-  
 619 nished by smaller  $r_e$ , likely reflects a subsaturated layer where sublimation occurs. The ver-  
 620 tical structure of  $\alpha_v$  (not shown) is very similar to that of IWC; this is consistent with  
 621 the finding that the radiative properties of anvil clouds are shaped primarily by large  
 622 ice crystals (Jensen et al., 2009; Lawson et al., 2010).

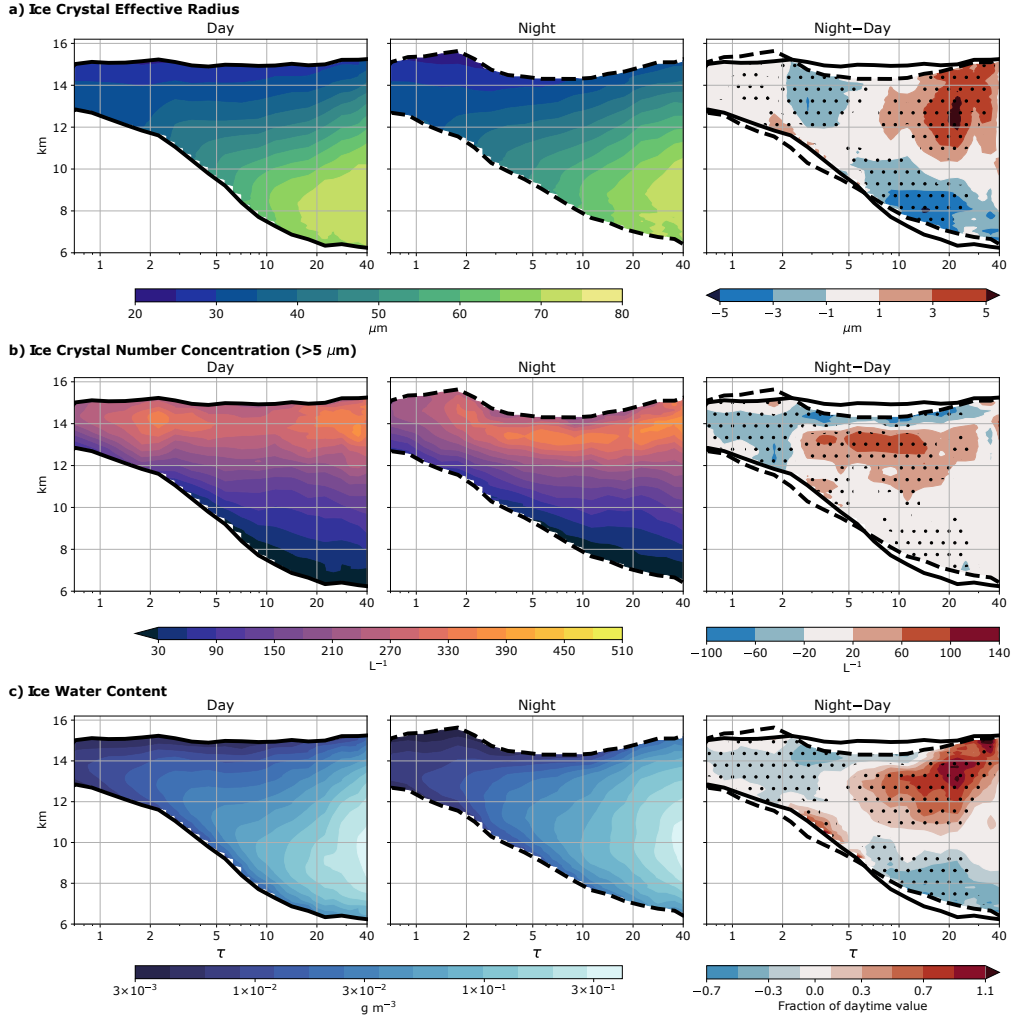


**Figure 8.** Composites of (a) effective radius, (b) number concentration of ice crystals with a maximum diameter exceeding  $5 \mu\text{m}$ , and (c) ice water content for anvil clouds in the West Pacific for (left) day, (middle) night, and (right) night minus day. Values are the means of the 100 subsample composites. Stippling indicates a statistically significant difference between day and night. Black lines (solid for day, dashed for night) indicate median CTH and CBH. In (c), the color shading for the day and night composites uses a logarithmic scale, and the night–day difference is expressed as a fraction of the daytime value.

623 There is large diurnal variability in the vertical structure of fresh, optically thick  
 624 anvils with  $\tau$  exceeding 10. They are more “top-heavy” at 01:30, in that  $r_e$ , IWC, and  
 625  $N_i$  are larger in the upper half of the cloud and smaller in the bottom half than they are  
 626 at 13:30. These differences are statistically significant in many areas. Since top-heaviness  
 627 would be expected to generally decrease with time as large ice crystals settle, it could

628 be the case that optically thick anvils observed at 01:30 were detrained more recently  
 629 than those observed at 13:30. It could also be the case that deep convection is more in-  
 630 tense at night and carries large ice crystals to higher altitudes. We cannot distinguish  
 631 these effects here but believe that the diurnal variability in the vertical structure of freshly  
 632 detrained anvils is worthy of further study.

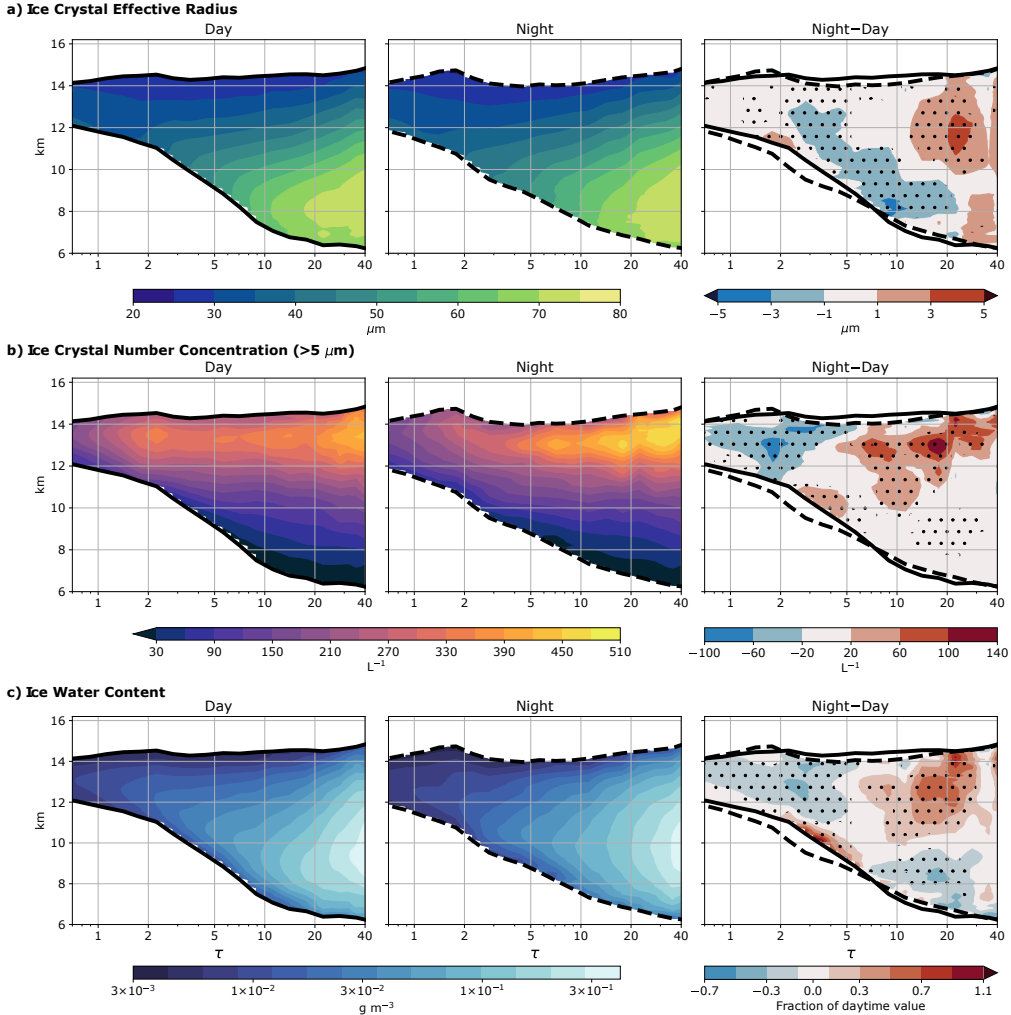


**Figure 9.** As in Figure 8, but for the Indian Ocean region.

633 As  $\tau$  decreases from 40 to 10, the IWC and  $r_e$  at a fixed altitude decrease substan-  
 634 tially. In Figures 8 and 9, this appears as positively sloped contours in the upper por-  
 635 tions of the cloud at large  $\tau$ . Cloud-top  $N_i$  also decreases, although the decrease is not  
 636 monotonic in every composite. This factor-of-four decrease in  $\tau$  is accompanied by a re-  
 637 latively small decrease in geometric thickness, suggesting that optical thinning at the ini-  
 638 tial stages of the anvil life cycle is driven primarily by microphysical changes rather than  
 639 geometric changes. This could reflect anvil precipitation and is consistent with previous  
 640 findings that large ice crystals are removed relatively rapidly after detrainment (Garrett  
 641 et al., 2005; Jensen et al., 2018). On the whole, these changes act to reduce the initial  
 642 diurnal difference in microphysical structure, though the 01:30 anvils remain more top-  
 643 heavy in some respects at  $\tau = 10$ .

644 As  $\tau$  falls below 10, the relative importance of geometric and microphysical thin-  
 645 ning shifts. At this point, geometric thickness begins to decrease rapidly with decreas-  
 646 ing  $\tau$ , and the  $r_e$  and IWC contours in the upper portion of the anvil flatten out. This  
 647 transition is most apparent in the 13:30 composite for the WP and is indicative of a mi-  
 648 crophysical equilibrium in which  $r_e$  and IWC remain relatively constant at a fixed alti-  
 649 tude level. A similar equilibrium was noted by Gallagher et al. (2012) during aircraft  
 650 sampling of convective outflow and was attributed to a balance between the growth of  
 651 ice crystals by agglomeration and their removal by sedimentation.

652 The evolution of cloud-top  $N_i$  as  $\tau$  decreases from 10 to 2 is of particular interest.  
 653 After its initial post-detrainment decrease,  $N_i$  reaches a relative minimum at some  $\tau$  be-  
 654 tween 3 and 7, depending on the region and time of day. As  $\tau$  reaches the modal range,  
 655 there is a resurgence in  $N_i$  that is present in all of the composites but is much more pro-  
 656 nounced during the day, when it peaks at  $\tau \approx 2.2$ . This coincides with the large day-  
 657 time increase in radiative LRT and  $\overline{Q}_R$  and the  $\sim 300$ -m increase in daytime median CTH.  
 658 At night, when there is no notable increase in LRT at the modal  $\tau$  but rather a large  
 659 rise in CTH, the  $N_i$  resurgence is much less pronounced, constituting only a minor dis-  
 660 ruption to the general decrease in cloud-top  $N_i$  that accompanies optical thinning. The  
 661 daytime resurgence in  $N_i$  is not sensitive to the compositing methodology described in  
 662 section 2.3, in which each composite reflects the median microphysical quantities of anvil  
 663 cloud profiles falling within a  $\tau$ -specific CTH and CBH range. If we instead compare all  
 664 13:30 anvil profiles with CTH within a fixed range, enhanced  $N_i$  is consistently found  
 665 in those with  $\tau$  between  $\sim 1.5$  and  $\sim 3$ . This ensures that the  $N_i$  signal at  $\tau \approx 2.2$  is not  
 666 a spurious result caused by the slight rise in daytime median CTH observed at that point,  
 667 which could affect the  $N_i$  retrieval via a decrease in temperature. The implications of  
 668 the  $N_i$  evolution observed here are discussed in the following section.

## 669 4 Discussion

670 The findings presented in section 3 offer strong support for the selective cloud main-  
 671 tenance hypothesis proposed by Hartmann and Berry (2017). Anvil clouds with an op-  
 672 tical depth between 1 and 2 (“modal anvils”) are especially abundant in convective re-  
 673 gions and are uniquely capable of persisting far from any convective core. This suggests  
 674 that the mechanisms that maintain anvil clouds are most active within the modal  $\tau$  range  
 675 and that optically thicker clouds will continue to thin until the modal  $\tau$  is reached. We  
 676 find that most of this thinning occurs within  $\sim 60$  km of the convective core, beyond which  
 677 the cloud distribution becomes increasingly dominated by modal anvils. Past work sug-  
 678 gests that the initial optical thinning is driven by dynamic outflow collapse (Lilly, 1988)  
 679 and by the fallout of large ice crystals (e.g., Gallagher et al., 2012; Jensen et al., 2018).  
 680 We find evidence for both of these mechanisms and hypothesize that radiative heating  
 681 can influence the thinning of freshly detrained anvils by hastening cloud-top subsidence  
 682 at night and hindering it during the day.

683 Our findings also offer insight into the physical mechanisms responsible for the main-  
 684 tenance of modal anvils. Modal anvils undergo stronger radiative heating and have higher  
 685 cloud tops than thicker anvils, which is consistent with the mesoscale lofting of the cloud  
 686 with respect to its clear-sky surroundings. However, it is puzzling that modal anvil tops  
 687 are found at lower altitudes during the day than at night despite the fact that there is  
 688 stronger radiative heating during the day. It is possible that most of the modal anvils  
 689 observed at 01:30 were detrained during the day, when solar heating would have hindered  
 690 cloud-top subsidence and geometric thinning. As they age, they could retain the higher  
 691 CTH and thicker geometry relative to anvils detrained at night (but observed at 13:30)  
 692 that underwent faster geometric thinning due to cloud-top cooling. This explanation sug-  
 693 gests that the life cycle of convective outflow is subject to hysteresis, in which the ini-  
 694 tial evolution of a freshly detrained cloud influences its properties later on. It could then  
 695 be the case that the large increase in 01:30 median CTH as  $\tau$  approaches the modal range

696 represents a shift in the anvil cloud population from those that were detrained at night  
697 to those detrained during the previous day.

698 Additionally, we find that the modal anvils observed at 13:30 are subjected to strong  
699 radiative destabilization and have higher cloud-top  $N_i$  than optically thicker clouds. This  
700 is consistent with the microphysical cycling mechanism of anvil maintenance, in which  
701 radiatively driven turbulence maintains or increases  $N_i$  by driving new ice crystal nu-  
702 cleation, counteracting sedimentation, or some combination thereof (Hartmann et al.,  
703 2018). It is also possible that the enhanced  $N_i$  is another example of the timing effect  
704 described previously: since anvils are detrained with higher  $N_i$  at night, the  $N_i$  resur-  
705 gence at modal  $\tau$  at 13:30 may simply reflect a transition from fresher, optically thick  
706 clouds detrained during the day to aged, thin clouds detrained during the the previous  
707 night. Even if this were the case, the high  $N_i$  in modal anvils would still reflect an im-  
708 pressive preservation of ice crystal number against sedimentation over large distances and  
709 timescales. The maintenance of cloud ice is also supported by our finding that  $r_e$  and  
710 IWC are approximately constant at a fixed altitude for  $\tau$  below  $\sim 5$ -10, most notably dur-  
711 ing the day. This suggests that the loss of ice due to gravity is being slowed and offers  
712 further support for the importance of in-cloud turbulence.

713 If destabilization is critical to cloud maintenance, it is possible that the thinner ge-  
714 ometry of modal anvils observed during the day results from natural selection. Thinner  
715 anvils would be better suited to withstand the stabilization imparted by solar heating,  
716 since LW destabilization is greater in thinner clouds than in thicker clouds of equal  $\tau$ .  
717 At night, in the absence of solar heating, such a thin geometry would not be required  
718 to achieve the same net destabilization. It may be that the diurnal difference in anvil  
719 structure results partly from this selection and partly from the hysteresis described pre-  
720 viously.

721 Past work provides a theoretical framework for understanding the relative impor-  
722 tance of mesoscale lofting and in-cloud convective mixing in the cirrus response to ra-  
723 diative heating. Mixing is favored over lofting when the cloud is horizontally extensive,  
724 cloud-base  $Q_R$  is strong, and the static stability of the environment is low (Garrett et  
725 al., 2005; Schmidt & Garrett, 2013). Modal anvils are wider than freshly detrained anvils  
726 and undergo especially strong heating at cloud base during the day. Furthermore, their  
727 typical CBH of  $\sim 12$  km coincides with a relative minimum in static stability, as calcu-  
728 lated from ERA-Interim reanalysis for the study region. For these reasons, modal anvils  
729 may be more susceptible to in-cloud convection than their fresh, optically thick precu-  
730 sors, which are narrower and are surrounded at their bases by a more stable environment.  
731 Following Garrett et al. (2005), the relative importance of the two mechanisms can be  
732 determined by the ratio  $Q_R L / N h^2 (d\theta/dz)$ , where  $L$  is the anvil half-width,  $N$  is the en-  
733 vironmental buoyancy frequency,  $h$  is the depth of the heated layer at cloud base, and  
734  $\theta$  is potential temperature. Our results indicate that  $h$  is on the order of  $\sim 1$  km, and typ-  
735 ical values of  $N$  ( $0.009 \text{ s}^{-1}$ ) and  $d\theta/dz$  ( $3 \text{ K km}^{-1}$ ) are derived from ERA-Interim re-  
736 analysis. We test a range of values for  $Q_R$  between 10 and 20  $\text{K day}^{-1}$  and for  $L$  between  
737 20 and 100 km and find that the ratio falls between 0.1 and 0.9. This suggests that both  
738 mesoscale lofting and in-cloud convection play important roles in the anvil response to  
739 radiative heating.

740 While this study has focused on radiative heating as a driver of anvil cloud evo-  
741 lution, it is important to remember that other processes are at play. Numerical models  
742 indicate that latent heating is substantial, especially at the edges of freshly detrained anvils  
743 where ice crystals can readily sublime (Gasparini et al., 2019). Additionally, anvil clouds  
744 may respond to radiative heating in ways not discussed here. For example, Schmidt and  
745 Garrett (2013) found that tenuous cirrus clouds may evaporate in response to radiative  
746 heating, especially when there is high static stability.

## 5 Summary and Conclusions

We have provided a observational assessment of the macrophysical and microphysical evolution of tropical anvil clouds. Clouds associated with deep convection impart a distinct signature on the climatological distribution of cloud layer IWP that allows them to be distinguished from the thin cirrus clouds that blanket the tropical upper troposphere. Using a combined radar-lidar retrieval, we find that cirrus clouds layers with  $1 < \tau < 2$  (“modal anvils”) are especially prevalent across two maritime convective regions. Modal anvils have the following characteristics:

- They can persist several hundred kilometers away from a convective core and dominate the anvil cloud distribution at spreading distances greater than  $\sim 60$  km.
- They have higher cloud tops than optically thicker anvils. This lofting is especially pronounced at night.
- They are subjected to stronger net radiative heating than optically thick anvils. Modal anvils undergo LW heating throughout their entirety, whereas optically thicker clouds experience cloud-top cooling.
- They are geometrically thinner at 13:30 than at 01:30, with a 600-m difference in median thickness. The thinner geometry of modal anvils observed during the day renders them particularly prone to radiative destabilization.
- This daytime destabilization is associated with enhanced  $N_i$  at cloud top. At night, when modal anvils are geometrically thicker and less susceptible to radiative destabilization, the  $N_i$  resurgence is correspondingly weaker.

These findings are in agreement with the hypothesis that anvil clouds with a positive NCRE are selectively maintained by radiative heating. They are also consistent with two proposed mechanisms of anvil maintenance: microphysical cycling, in which radiatively driven turbulence prevents the depletion of cloud ice, and mesoscale lofting, in which the cloud as a whole rises with respect to its surroundings. We have further hypothesized that the properties of aged anvil clouds are determined in part by the time of day at which they were first detrained. The rapid geometric thinning of anvil clouds detrained at night may facilitate stronger radiative heating and destabilization later on. Meanwhile, the slower thinning of anvil clouds detrained during the day allows their tops to persist at higher altitudes but results in weaker heating. Hysteresis could have important implications for anvil cloud evolution in a changing climate and is worthy of further study using cloud-resolving models that include a realistic diurnal cycle of insolation.

The present study underscores the importance of radiative, dynamic, and microphysical processes in determining the NCRE in tropical convective regions. Future work should focus on how the cloud maintenance processes examined here interact with other changes that are expected to result from greenhouse gas warming. In a warmer world, tropical convection is expected to be more aggregated (Emanuel et al., 2014), and anvil clouds are expected to move upwards in altitude (Hartmann & Larson, 2002), where they may encounter an increasingly stable environment (Zelinka & Hartmann, 2010). The impact of these changes on high cloud fraction remains uncertain, with some models predicting varying degrees of reduction (Tompkins & Craig, 1999; Bony et al., 2016; Li et al., 2019) and others predicting an increase (Ohno et al., 2019). Discussions of future anvil cloud amount have typically focused on changes in the amount of convective detrainment; our results show that post-detrainment maintenance processes must also be considered.

## Acknowledgments

Support for this research was provided by the National Science Foundation under grant AGS-1549579. We acknowledge Blaž Gasparini and Casey Wall for comments and

796 insightful discussions that improved this work. We thank Tim Garrett, two anonymous  
 797 reviewers, and an associate editor for their constructive comments. DARDAR data was  
 798 obtained from the ICARE Data and Services Center (<http://www.icare.univ-lille1.fr/projects/dardar>)  
 799 and MODIS data from the NASA Level-1 and Atmosphere Archive and Distribution Sys-  
 800 tem (<https://ladsweb.modaps.eosdis.nasa.gov>). The derived data and radiative heating  
 801 model results needed to reproduce the figures in this paper are available at <http://hdl.handle.net/1773/45556>.

## 802 References

- 803 Ackerman, T. P., Liou, K. N., Valero, F. P., & Pfister, L. (1988). Heating rates in  
 804 tropical anvils. *Journal of the Atmospheric Sciences*, *45*(10), 1606–1623. doi:  
 805 10.1175/1520-0469(1988)045<1606:HRITA>2.0.CO;2
- 806 Berry, E., & Mace, G. G. (2014, 8). Cloud properties and radiative effects of the  
 807 Asian summer monsoon derived from A-Train data. *Journal of Geophysical Re-*  
 808 *search*, *119*(15), 9492–9508. doi: 10.1002/2014JD021458
- 809 Bony, S., Stevens, B., Coppin, D., Becker, T., Reed, K. A., Voigt, A., & Medeiros,  
 810 B. (2016). Thermodynamic control of anvil cloud amount. *Proceedings*  
 811 *of the National Academy of Sciences of the United States of America*. doi:  
 812 10.1073/pnas.1601472113
- 813 Bretherton, C. S., Blossey, P. N., & Khairoutdinov, M. (2005). An energy-balance  
 814 analysis of deep convective self-aggregation above uniform SST. *Journal of the*  
 815 *Atmospheric Sciences*. doi: 10.1175/JAS3614.1
- 816 Cazenave, Q., Ceccaldi, M., Delanoë, J., Pelon, J., Groß, S., & Heymsfield, A. (2019,  
 817 5). Evolution of DARDAR-CLOUD ice cloud retrievals: New parameters and  
 818 impacts on the retrieved microphysical properties. *Atmospheric Measurement*  
 819 *Techniques*, *12*(5), 2819–2835. doi: 10.5194/amt-12-2819-2019
- 820 Delanoë, J., & Hogan, R. J. (2008, 4). A variational scheme for retrieving ice cloud  
 821 properties from combined radar, lidar, and infrared radiometer. *Journal of*  
 822 *Geophysical Research Atmospheres*, *113*(7). doi: 10.1029/2007JD009000
- 823 Delanoë, J., & Hogan, R. J. (2010). Combined CloudSat-CALIPSO-MODIS re-  
 824 trievals of the properties of ice clouds. *Journal of Geophysical Research Atmo-*  
 825 *spheres*, *115*(4). doi: 10.1029/2009JD012346
- 826 Delanoë, J., Protat, A., Jourdan, O., Pelon, J., Papazzoni, M., Dupuy, R., . . .  
 827 Jouan, C. (2013, 1). Comparison of Airborne In Situ, Airborne Radar–Lidar,  
 828 and Spaceborne Radar–Lidar Retrievals of Polar Ice Cloud Properties Sam-  
 829 pled during the POLARCAT Campaign. *Journal of Atmospheric and Oceanic*  
 830 *Technology*, *30*(1), 57–73. doi: 10.1175/JTECH-D-11-00200.1
- 831 Deng, M., Mace, G. G., Wang, Z., & Paul Lawson, R. (2013). Evaluation of several  
 832 A-Train ice cloud retrieval products with in situ measurements collected during  
 833 the SPARTICUS campaign. *Journal of Applied Meteorology and Climatology*.  
 834 doi: 10.1175/JAMC-D-12-054.1
- 835 Dinh, T. P., Durran, D. R., & Ackerman, T. P. (2010, 1). Maintenance of tropi-  
 836 cal tropopause layer cirrus. *Journal of Geophysical Research*, *115*(D2),  
 837 D02104. Retrieved from <http://doi.wiley.com/10.1029/2009JD012735>  
 838 doi: 10.1029/2009JD012735
- 839 Dobbie, S., & Jonas, P. (2001, 10). Radiative influences on the structure and life-  
 840 time of cirrus clouds. *Quarterly Journal of the Royal Meteorological Society*,  
 841 *127*(578), 2663–2682. doi: 10.1002/qj.49712757808
- 842 Durran, D. R., Dinh, T., Ammerman, M., & Ackerman, T. (2009, 9). The mesoscale  
 843 dynamics of thin tropical tropopause cirrus. *Journal of the Atmospheric Sci-*  
 844 *ences*, *66*(9), 2859–2873. Retrieved from [http://journals.ametsoc.org/](http://journals.ametsoc.org/jas/article-pdf/66/9/2859/3515414/2009jas3046_1.pdf)  
 845 [jas/article-pdf/66/9/2859/3515414/2009jas3046\\_1.pdf](http://journals.ametsoc.org/jas/article-pdf/66/9/2859/3515414/2009jas3046_1.pdf) doi: 10.1175/  
 846 2009JAS3046.1
- 847 Emanuel, K., Wing, A. A., & Vincent, E. M. (2014). Radiative-convective in-  
 848 stability. *Journal of Advances in Modeling Earth Systems*. doi: 10.1002/

- 849 2013MS000270
- 850 Fu, Q. (1996, 9). An accurate parameterization of the solar radiative proper-  
 851 ties of cirrus clouds for climate models. *Journal of Climate*, 9(9), 2058–  
 852 2082. Retrieved from [http://journals.ametsoc.org/jcli/article-pdf/](http://journals.ametsoc.org/jcli/article-pdf/9/9/2058/4701742/1520-0442)  
 853 [9/9/2058/4701742/1520-0442](http://journals.ametsoc.org/jcli/article-pdf/9/9/2058/4701742/1520-0442) doi: 10.1175/1520-0442(1996)009<2058:  
 854 AAPOTS>2.0.CO;2
- 855 Fu, Q., Yang, P., & Sun, W. B. (1998, 9). An Accurate Parameterization of the  
 856 Infrared Radiative Properties of Cirrus Clouds for Climate Models. *Journal of*  
 857 *Climate*, 11(9), 2223–2237. doi: 10.1175/1520-0442(1998)011<2223:AAPOTI>2  
 858 .0.CO;2
- 859 Gallagher, M. W., Connolly, P. J., Crawford, I., Heymsfield, A., Bower, K. N.,  
 860 Choulaton, T. W., ... Hacker, J. (2012, 7). Observations and modelling of  
 861 microphysical variability, aggregation and sedimentation in tropical anvil cirrus  
 862 outflow regions. *Atmospheric Chemistry and Physics*, 12(14), 6609–6628. doi:  
 863 10.5194/acp-12-6609-2012
- 864 Garrett, T. J., Navarro, B. C., Twohy, C. H., Jensen, E. J., Baumgardner, D. G.,  
 865 Bui, P. T., ... Weinstock, E. M. (2005, 7). Evolution of a Florida cirrus anvil.  
 866 *Journal of the Atmospheric Sciences*, 62(7 II), 2352–2372. Retrieved from  
 867 [http://journals.ametsoc.org/jas/article-pdf/62/7/2352/3485107/](http://journals.ametsoc.org/jas/article-pdf/62/7/2352/3485107/jas3495.1.pdf)  
 868 [jas3495.1.pdf](http://journals.ametsoc.org/jas/article-pdf/62/7/2352/3485107/jas3495.1.pdf) doi: 10.1175/JAS3495.1
- 869 Gasparini, B., Blossey, P. N., Hartmann, D. L., Lin, G., & Fan, J. (2019, 7). What  
 870 drives the lifecycle of tropical anvil clouds? *Journal of Advances in Modeling*  
 871 *Earth Systems*, 2019MS001736. doi: 10.1029/2019MS001736
- 872 Gettelman, A., Salby, M. L., & Sassi, F. (2002, 5). Distribution and influence of con-  
 873 vection in the tropical tropopause region. *Journal of Geophysical Research D:*  
 874 *Atmospheres*, 107(9-10), 6–1. doi: 10.1029/2001jd001048
- 875 Harrison, E. F., Minnis, P., Barkstrom, B. R., Ramanathan, V., Cess, R. D., & Gib-  
 876 son, G. G. (1990). Seasonal variation of cloud radiative forcing derived from  
 877 the Earth Radiation Budget Experiment. *Journal of Geophysical Research*,  
 878 95(D11). doi: 10.1029/jd095id11p18687
- 879 Hartmann, D. L. (2016). *Tropical anvil clouds and climate sensitivity*. doi: 10.1073/  
 880 pnas.1610455113
- 881 Hartmann, D. L., & Berry, S. E. (2017). The balanced radiative effect of tropical  
 882 anvil clouds. *Journal of Geophysical Research*, 122(9), 5003–5020. doi: 10  
 883 .1002/2017JD026460
- 884 Hartmann, D. L., Gasparini, B., Berry, S. E., & Blossey, P. N. (2018, 12). The Life  
 885 Cycle and Net Radiative Effect of Tropical Anvil Clouds. *Journal of Advances*  
 886 *in Modeling Earth Systems*, 10(12), 3012–3029. doi: 10.1029/2018MS001484
- 887 Hartmann, D. L., & Larson, K. (2002). An important constraint on tropical cloud -  
 888 climate feedback. *Geophysical Research Letters*. doi: 10.1029/2002gl015835
- 889 Hartmann, D. L., Moy, L. A., & Fu, Q. (2001). Tropical convection and the energy  
 890 balance at the top of the atmosphere. *Journal of Climate*. doi: 10.1175/1520  
 891 -0442(2001)014<4495:TCATEB>2.0.CO;2
- 892 Heymsfield, A. J., Bansemer, A., Field, P. R., Durden, S. L., Stith, J. L., Dye,  
 893 J. E., ... Grainger, C. A. (2002). Observations and parameterizations  
 894 of particle size distributions in deep tropical cirrus and stratiform pre-  
 895 cipitating clouds: Results from in situ observations in TRMM field cam-  
 896 paigns. *Journal of the Atmospheric Sciences*, 59(24), 3457–3491. doi:  
 897 10.1175/1520-0469(2002)059<3457:OAPOPS>2.0.CO;2
- 898 Iacono, M. J., Mlawer, E. J., Clough, S. A., & Morcrette, J.-J. (2000, 6). Impact  
 899 of an improved longwave radiation model, RRTM, on the energy budget and  
 900 thermodynamic properties of the NCAR community climate model, CCM3.  
 901 *Journal of Geophysical Research: Atmospheres*, 105(D11), 14873–14890. doi:  
 902 10.1029/2000JD900091
- 903 Igel, M. R., Drager, A. J., & van den Heever, S. C. (2014, 9). A CloudSat cloud ob-

- 904       ject partitioning technique and assessment and integration of deep convective  
 905       anvil sensitivities to sea surface temperature. *Journal of Geophysical Research:*  
 906       *Atmospheres*, 119(17), 10515–10535. doi: 10.1002/2014JD021717
- 907 Järvinen, E., Jourdan, O., Neubauer, D., Yao, B., Liu, C., Andreae, M. O., ...  
 908 Schnaiter, M. (2018, 11). Additional global climate cooling by clouds due to  
 909 ice crystal complexity. *Atmospheric Chemistry and Physics*, 18(21), 15767–  
 910 15781. Retrieved from <https://www.atmos-chem-phys.net/18/15767/2018/>  
 911 doi: 10.5194/acp-18-15767-2018
- 912 Jensen, E. J., Lawson, P., Baker, B., Pilon, B., Mo, Q., Heymsfield, A. J., ...  
 913 Tanelli, S. (2009). On the importance of small ice crystals in tropical anvil  
 914 cirrus. *Atmospheric Chemistry and Physics*. doi: 10.5194/acp-9-5519-2009
- 915 Jensen, E. J., van den Heever, S. C., & Grant, L. D. (2018, 9). The Life Cy-  
 916 cles of Ice Crystals Detrained From the Tops of Deep Convection. *Jour-*  
 917 *nal of Geophysical Research: Atmospheres*, 123(17), 9624–9634. doi:  
 918 10.1029/2018JD028832
- 919 Krämer, M., Rolf, C., Spelten, N., Afchine, A., Fahey, D., Jensen, E., ... Sourdeval,  
 920 O. (2020). A Microphysics Guide to Cirrus – Part II: Climatologies of Clouds  
 921 and Humidity from Observations. *Atmospheric Chemistry and Physics*, 1–63.  
 922 doi: 10.5194/acp-2020-40
- 923 Lawson, R. P., Jensen, E., Mitchell, D. L., Baker, B., Mo, Q., & Pilon, B. (2010).  
 924 Microphysical and radiative properties of tropical clouds investigated in TC4  
 925 and NAMMA. *Journal of Geophysical Research*. doi: 10.1029/2009jd013017
- 926 Li, R. L., Storelvmo, T., Fedorov, A. V., & Choi, Y.-S. (2019, 8). A Positive Iris  
 927 Feedback: Insights from Climate Simulations with Temperature-Sensitive  
 928 Cloud–Rain Conversion. *Journal of Climate*, 32(16), 5305–5324. doi:  
 929 10.1175/JCLI-D-18-0845.1
- 930 Lilly, D. K. (1988). Cirrus outflow dynamics. *Journal of the Atmospheric Sciences*,  
 931 45(10), 1594–1605. doi: 10.1175/1520-0469(1988)045<1594:COD>2.0.CO;2
- 932 Luo, Z., & Rossow, W. B. (2004, 12). Characterizing Tropical Cirrus Life Cycle,  
 933 Evolution, and Interaction with Upper-Tropospheric Water Vapor Using La-  
 934 grangian Trajectory Analysis of Satellite Observations. *Journal of Climate*,  
 935 17(23), 4541–4563. doi: 10.1175/3222.1
- 936 Mace, G. G., Deng, M., Soden, B., & Zipser, E. (2006, 2). Association of tropi-  
 937 cal cirrus in the 10-15-km layer with deep convective sources: An Observa-  
 938 tional study combining millimeter radar data and satellite-derived trajecto-  
 939 ries. *Journal of the Atmospheric Sciences*, 63(2), 480–503. Retrieved from  
 940 [http://journals.ametsoc.org/jas/article-pdf/63/2/480/3488198/](http://journals.ametsoc.org/jas/article-pdf/63/2/480/3488198/jas3627.1.pdf)  
 941 [jas3627.1.pdf](http://journals.ametsoc.org/jas/article-pdf/63/2/480/3488198/jas3627.1.pdf) doi: 10.1175/JAS3627.1
- 942 Massie, S., Gettelman, A., Randel, W., & Baumgardner, D. (2002, 11). Distri-  
 943 bution of tropical cirrus in relation to convection. *Journal of Geophysical Re-*  
 944 *search: Atmospheres*, 107(D21), 19–1. doi: 10.1029/2001JD001293
- 945 McFarquhar, G. M., & Heymsfield, A. J. (1996, 9). Microphysical Character-  
 946 istics of Three Anvils Sampled during the Central Equatorial Pacific Ex-  
 947 periment. *Journal of the Atmospheric Sciences*, 53(17), 2401–2423. doi:  
 948 10.1175/1520-0469(1996)053<2401:MCOTAS>2.0.CO;2
- 949 McFarquhar, G. M., Heymsfield, A. J., Spinhirne, J., & Hart, B. (1999, 6). Thin  
 950 and Subvisual Tropopause Tropical Cirrus: Observations and Radiative  
 951 Impacts. *Journal of the Atmospheric Sciences*, 57(12), 1841–1853. doi:  
 952 10.1175/1520-0469(2000)057<1841:TASTTC>2.0.CO;2
- 953 McGill, M. J., Vaughan, M. A., Trepte, C. R., Hart, W. D., Hlavka, D. L., Winker,  
 954 D. M., & Kuehn, R. (2007, 10). Airborne validation of spatial properties  
 955 measured by the CALIPSO lidar. *Journal of Geophysical Research*, 112(D20),  
 956 D20201. doi: 10.1029/2007JD008768
- 957 Mlawer, E. J., Taubman, S. J., Brown, P. D., Iacono, M. J., & Clough, S. A. (1997,  
 958 7). Radiative transfer for inhomogeneous atmospheres: RRTM, a validated

- 959 correlated-k model for the longwave. *Journal of Geophysical Research: Atmo-*  
 960 *spheres*, 102(D14), 16663–16682. doi: 10.1029/97JD00237
- 961 Nesbitt, S. W., & Zipser, E. J. (2003, 5). The Diurnal Cycle of Rainfall and Con-  
 962 vective Intensity according to Three Years of TRMM Measurements. *Journal*  
 963 *of Climate*, 16(10), 1456–1475. doi: 10.1175/1520-0442-16.10.1456
- 964 Ohno, T., Satoh, M., & Noda, A. (2019, 6). Fine Vertical Resolution Radiative-  
 965 Convective Equilibrium Experiments: Roles of Turbulent Mixing on the  
 966 High-Cloud Response to Sea Surface Temperatures. *Journal of Advances in*  
 967 *Modeling Earth Systems*, 11(6), 1637–1654. doi: 10.1029/2019MS001704
- 968 Platnick, S., Meyer, K. G., King, M. D., Wind, G., Amarasinghe, N., Marchant,  
 969 B., ... Riedi, J. (2017, 1). The MODIS Cloud Optical and Microphys-  
 970 ical Products: Collection 6 Updates and Examples from Terra and Aqua.  
 971 *IEEE Transactions on Geoscience and Remote Sensing*, 55(1), 502–525. doi:  
 972 10.1109/TGRS.2016.2610522
- 973 Ramanathan, V., Cess, R. D., Harrison, E. F., Minnis, P., Barkstrom, B. R., Ah-  
 974 mad, E., & Hartmann, D. (1989). Cloud-radiative forcing and climate: Results  
 975 from the earth radiation budget experiment. *Science*, 243(4887), 57–63. doi:  
 976 10.1126/science.243.4887.57
- 977 Randall, D. A., Harshvardhan, Dazlich, D. A., & Corsetti, T. G. (1989). In-  
 978 teractions among radiation, convection, and large-scale dynamics in a  
 979 general circulation model. *Journal of the Atmospheric Sciences*. doi:  
 980 10.1175/1520-0469(1989)046<1943:IARCAL>2.0.CO;2
- 981 Schmidt, C. T., & Garrett, T. J. (2013). A Simple Framework for the Dynamic  
 982 Response of Cirrus Clouds to Local Diabatic Radiative Heating. *Journal of the*  
 983 *Atmospheric Sciences*, 70(5), 1409–1422. doi: 10.1175/JAS-D-12-056.1
- 984 Setvák, M., Rabin, R. M., & Wang, P. K. (2006). Contribution of the MODIS in-  
 985 strument to observations of deep convective storms and stratospheric moisture  
 986 detection in GOES and MSG imagery.  
 987 doi: 10.1016/j.atmosres.2005.09.015
- 988 Sourdeval, O., Gryspeerdt, E., Krämer, M., Goren, T., Delanoë, J., Afchine, A., ...  
 989 Quaas, J. (2018). Ice crystal number concentration estimates from lidar-radar  
 990 satellite remote sensing-Part 1: Method and evaluation. *Atmos. Chem. Phys*,  
 991 18, 14327–14350. doi: 10.5194/acp-18-14327-2018
- 992 Stein, T. H. M., Delanoë, J., & Hogan, R. J. (2011, 9). A Comparison among  
 993 Four Different Retrieval Methods for Ice-Cloud Properties Using Data from  
 994 CloudSat , CALIPSO , and MODIS. *Journal of Applied Meteorology and*  
 995 *Climatology*, 50(9), 1952–1969. doi: 10.1175/2011JAMC2646.1
- 996 Stephens, G. L., Vane, D. G., Boain, R. J., Mace, G. G., Sassen, K., Wang, Z.,  
 997 ... Mitrescu, C. (2002, 12). The cloudsat mission and the A-Train: A  
 998 new dimension of space-based observations of clouds and precipitation.  
 999 *Bulletin of the American Meteorological Society*, 83(12), 1771–1790. doi:  
 1000 10.1175/BAMS-83-12-1771
- 1001 Tompkins, A. M., & Craig, G. C. (1999). Sensitivity of tropical convection to sea  
 1002 surface temperature in the absence of large-scale flow. *Journal of Climate*. doi:  
 1003 10.1175/1520-0442(1999)012<0462:SOTCTS>2.0.CO;2
- 1004 Voigt, A., & Shaw, T. A. (2015). Circulation response to warming shaped by ra-  
 1005 diative changes of clouds and water vapour. *Nature Geoscience*. doi: 10.1038/  
 1006 ngeo2345
- 1007 Wall, C. J., Hartmann, D. L., & Norris, J. R. (2019, 10). Is the net cloud radiative  
 1008 effect constrained to be uniform over the tropical warm pools? *Geophysical Re-*  
 1009 *search Letters*, 2019GL083642. doi: 10.1029/2019GL083642
- 1010 Wall, C. J., Hartmann, D. L., Thieman, M. M., Smith, W. L., & Minnis, P. (2018,  
 1011 12). The life cycle of anvil clouds and the top-of-atmosphere radiation balance  
 1012 over the tropical west Pacific. *Journal of Climate*, 31(24), 10059–10080. doi:  
 1013 10.1175/JCLI-D-18-0154.1

- 1014 Wendisch, M., Yang, P., & Pilewskie, P. (2007, 4). Effects of ice crystal habit on  
1015 thermal infrared radiative properties and forcing of cirrus. *Journal of Geophys-*  
1016 *ical Research*, *112*(D8), D08201. Retrieved from <http://doi.wiley.com/10>  
1017 [.1029/2006JD007899](http://doi.wiley.com/10.1029/2006JD007899) doi: 10.1029/2006JD007899
- 1018 Wing, A. A., & Emanuel, K. A. (2014). Physical mechanisms controlling self-  
1019 aggregation of convection in idealized numerical modeling simulations. *Journal*  
1020 *of Advances in Modeling Earth Systems*. doi: 10.1002/2013MS000269
- 1021 Winker, D. M., Pelon, J., Coakley, J. A., Ackerman, S. A., Charlson, R. J., Co-  
1022 larco, P. R., . . . Wielicki, B. A. (2010, 3). The CALIPSO Mission. *Bul-*  
1023 *letin of the American Meteorological Society*, *91*(9), 1211–1230. doi:  
1024 [10.1175/2010BAMS3009.1](http://doi.wiley.com/10.1175/2010BAMS3009.1)
- 1025 Winker, D. M., & Trepte, C. R. (1998, 9). Laminar cirrus observed near the tropical  
1026 tropopause by LITE. *Geophysical Research Letters*, *25*(17), 3351–3354. doi: 10  
1027 [.1029/98GL01292](http://doi.wiley.com/10.1029/98GL01292)
- 1028 Young, A. H., Bates, J. J., & Curry, J. A. (2012, 7). Complementary use of pas-  
1029 sive and active remote sensing for detection of penetrating convection from  
1030 CloudSat, CALIPSO, and Aqua MODIS. *Journal of Geophysical Research:*  
1031 *Atmospheres*, *117*(D13). doi: 10.1029/2011JD016749
- 1032 Yuan, J., & Houze, R. A. (2010). Global variability of mesoscale convective system  
1033 anvil structure from A-train satellite data. *Journal of Climate*, *23*(21), 5864–  
1034 5888. doi: 10.1175/2010JCLI3671.1
- 1035 Yuan, J., Houze, R. A., & Heymsfield, A. J. (2011). Vertical structures of anvil  
1036 clouds of tropical mesoscale convective systems observed by CloudSat. *Journal*  
1037 *of the Atmospheric Sciences*, *68*(8), 1653–1674. doi: 10.1175/2011JAS3687.1
- 1038 Zelinka, M. D., & Hartmann, D. L. (2010). Why is longwave cloud feedback posi-  
1039 tive? *Journal of Geophysical Research Atmospheres*, *115*(16). doi: 10.1029/  
1040 [2010JD013817](http://doi.wiley.com/10.1029/2010JD013817)